

**Investigation of Skin Dynamic Response after Precise Multiphoton-Thermolysis Using
Non-invasive Multimodality Microscopy and Imaging-guided Micro-Raman Spectroscopy**

by

Shujian Li

H.B.Sc., University of Toronto, 2018

A THESIS SUBMITTED IN PARTIAL FULFILLMENT OF
THE REQUIREMENTS FOR THE DEGREE OF

MASTER OF SCIENCE

in

THE FACULTY OF GRADUATE AND POSTDOCTORAL STUDIES
(Interdisciplinary Oncology)

THE UNIVERSITY OF BRITISH COLUMBIA
(Vancouver)

October 2021

© Shujian Li, 2021

The following individuals certify that they have read, and recommend to the Faculty of Graduate and Postdoctoral Studies for acceptance, a thesis entitled:

Investigation of Skin Dynamic Response after Precise Multiphoton-Thermolysis Using Non-invasive Multimodality Microscopy and Imaging-guided Micro-Raman Spectroscopy

submitted by Shujian Li in partial fulfillment of the requirements for

the degree of Master of Science

in Interdisciplinary Oncology

Examining Committee:

Dr. Haishan Zeng, Department of Dermatology and Skin Science, UBC

Supervisor

Dr. Harvey Lui, Department of Dermatology and Skin Science, UBC

Supervisory Committee Member

Dr. Sunil Kalia, Department of Dermatology and Skin Science, UBC

Supervisory Committee Member

Dr. Pierre Lane, Interdisciplinary Oncology Program, UBC

Additional Examiner

Abstract

The ability to restore tissue architecture and function after an injury is critical to health maintenance. Most studies investigate in this field of research are based on *ex vivo* histologic samples or genetic analysis of tissue biopsies. Previously in our lab, a real-time multimodality imaging system was developed for continuous monitoring of the exact same microscopic location for skin cellular dynamics. Meanwhile, a new laser therapy technique termed, multiphoton-thermolysis, was developed to achieve precise micro-alteration of skin without affecting the surrounding untargeted tissues. However, multiphoton-thermolysis has not yet been utilized in human skin *in vivo*. The objective of this thesis was to demonstrate the capability of multiphoton-thermolysis to induce precise skin alteration on human subject and to test the ability of our multimodality microscopy in monitoring skin dynamics *in vivo* following laser exposure. In this study, five volunteers were recruited, each of the volunteers received two multiphoton-thermolysis sessions on their inner forearm. The following skin response was monitored with the multimodality imaging system which integrates reflectance confocal microscopy (RCM), two-photon excitation fluorescence microscopy (TPF), and second harmonic generation microscopy (SHG) to provide complementary tissue information. Concurrently, an imaging-guided micro-Raman spectroscopy (IMRS) was also incorporated into this system to measure any biochemical changes during the recovery period. Each volunteer was measured at 8 time points, including: before, immediately after, 3 hours, 1 days, 3 days, 1 week, 2 weeks, and 4 weeks after the laser exposure. The results revealed that cellular response, including oncosis, necrosis, and inflammation, and tissue architectural modification including dermal remodeling after laser exposure were all successfully recorded using the multimodality imaging system. This pilot study shows that multiphoton-

thermolysis generates tissue alteration and initiates wound healing-like response in human subjects, which may provide a mechanism for treatment of skin conditions including skin cancers.

Lay Summary

The key objective of this study is to test the ability of a newly developed laser therapy to generate precise tissue alteration in human skin, and to demonstrate the efficiency of a prototype multimodal microscopy to monitor the skin responses after this laser exposure in real-time. Cellular activities such as proliferation, inflammation, exfoliation of injured tissue can be recorded over time. This study highlighted the potential use of this laser therapy in future clinical treatment for skin conditions that require precise targeting of the diseased tissue.

Preface

Research from this thesis was performed in the laboratory of Dr. Haishan Zeng at Vancouver General Hospital Research Pavilion and the BC Cancer Research Centre. All the experiments involving human subjects were approved by the University of British Columbia Research Ethics Board (Certificate #: H19-02318).

This thesis was conducted under supervision of Dr. Haishan Zeng. I was responsible for recruiting the volunteers, designing the procedure, conducting the experiments, and analyzing the research data.

Table of Contents

Abstract.....	iii
Lay Summary	v
Preface.....	vi
Table of Contents	vii
List of Figures.....	ix
List of Abbreviations	xi
Acknowledgements	xiii
Dedication	xiv
Chapter 1: Introduction	1
1.1 Basic of Skin Anatomy and Wound Healing.....	1
1.1.1 Basic Skin Structure.....	1
1.1.2 Wound Healing	2
1.2 Laser exposure and Non-invasive Measurements.....	5
1.2.1 Photothermolysis.....	5
1.2.2 Optical Imaging Techniques	8
1.2.2.1 Reflectance Confocal Microscopy	9
1.2.2.2 Two-Photon Excitation Microscopy	11
1.2.2.3 Second Harmonic Generation Microscopy.....	13
1.2.2.4 Raman Spectroscopy.....	14
1.2.2.5 Optical Redox Ratio.....	16
1.3 Objective and Hypothesis	17

Chapter 2: Materials and Methods	18
2.1 Study Design.....	18
2.2 System setup	20
2.3 Re-localization	25
2.4 Optical Redox Ratio.....	27
2.5 Measurements Procedure	28
2.6 Data analysis and processing	30
Chapter 3: Results and Discussion	31
3.1 Multiphoton Imaging	31
3.1.1 Epidermis	31
3.1.2 Dermis.....	42
3.2 Image-Guided Micro-Raman Spectroscopy	48
3.2.1 Epidermis	49
3.2.2 Dermis.....	53
3.3 Optical Redox Ratio.....	55
3.4 Conclusion	57
Bibliography	60

List of Figures

Figure 1. 1 Histology of a skin sample (a) and diagram illustrating the sequence of epidermal layers and different cell types (b)	2
Figure 1. 2 Schematics showing the concept of spatially selective photothermolysis. Multiphoton absorption only occurs at the focal point, as the photon density outside the focal point is low	7
Figure 1. 3 Schematic picture of basic set up of confocal microscope. Excitation light is shown in green and the emission light from the sample is shown in red.	11
Figure 1. 4 Schematic drawing illustrating the processes of fluorescence (left) single-photon fluorescence (right) two-photon fluorescence.	13
Figure 1. 5 Comparison of TPEF and SHG. In TPEF.	14
Figure 2. 1 System diagram of the in vivo multimodal microscopy that incorporated the IMRS (orange) and MPM (red) system.	24
Figure 2. 2 Clinical measurement set up of the imaging head.....	24
Figure 2. 3 Surface marker design.	26
Figure 3. 1 In vivo En-face MPM images of epidermis (laser exposure generated in the Stratum Spinosum) at different time points.	33
Figure 3. 2 Cross-sectional images of the laser exposed site at the stratum spinosum layer at different time points.....	34
Figure 3. 3 In vivo En-face MPM images of epidermis (laser exposure generated in the Stratum Basale) at different time points at different depths.....	36
Figure 3. 4 Cross-sectional images of the laser exposed site at the stratum basale layer at different time points.....	37

Figure 3. 5 En-face MPM images of the targeted site located in dermis.....	44
Figure 3. 6 Cross-sectional MPM images of the targeted site in dermis.	45
Figure 3. 7. Raman spectra at the laser exposed site in the epidermis before and after the laser exposure.....	49
Figure 3. 8 Raman spectra at the laser exposed site in the epidermis immediately after and at day 1 following the laser exposure.	51
Figure 3. 9 Raman spectra at the laser exposed site in the dermis before and immediately after the laser exposure.....	53
Figure 3. 10 Raman spectra at the laser exposed site in the dermis immediately after and at day 1 following the laser exposure.	54
Figure 3. 11 Average redox ratio of the basal cell layer for each volunteer at different time points.....	55
Figure 3. 12 Representative optical redox images of basal layer epidermis.....	57

List of Abbreviations

APD	Avalanche photodiode
CW	Continuous Wave
DM	Dichroic mirror
FAD	Flavin adenine dinucleotide
FOV	Field of View
<i>fs</i>	Femtosecond
FOV	Field of View
HWP	Half wave plate
IL-1 β	Interleukin-1 β
IMRS	Imaging-guided Micro-Raman Spectroscopy
L	Lens
LP	Long pass
M	Mirror
MEND	Microscopic Epidermal Necrotic Debris
MMPs	Matrix metalloproteinases
MPM	Multiphoton microscopy
NADH	Reduced nicotinamide adenine dinucleotide
PBS	Polarization beam splitter
PMT	Photomultiplier tube
QWP	Quarter wave plate
RCM	Reflectance Confocal Microscopy

ROS	Reactive oxygen species
SB	Stratum Basale
SC	Stratum Corneum
SG	Stratum Granulosum
SHG	Second Harmonic generation
SL	Stratum Lucidum
SP	Short pass
SS	Stratum Spinosum
TNF- α	Tissue necrotic factor- α
TPF	Two photon fluorescence
UV	Ultraviolet

Acknowledgements

I would like to express my sincere gratitude to my supervisor Dr. Haishan Zeng, whose guidance and support throughout my graduate studies made all this work possible. Graduate school under his supervision was an invaluable experience. I very much appreciate the opportunities he has given me. Especially during the pandemic, his warmed caring and suggestions for my project have encouraged me to persist in this difficult time.

I would also like to extend my gratitude to my committee members, Dr. Harvey Lui and Dr. Sunil Kalia for their useful insights and suggestions for my project. Their generous encouragement and support kept me motivated and determined. It was a very pleasant experience to work in this group, I want to thank all group members for creating such positive atmosphere. Special thank you goes to Dr. Jianhua Zhao, Dr. Zhenguo Wu, and Dr. Yunxian Tian, for their generous sharing of their rich research experience, and technical help.

Special thanks are owed to my parents, who have provided both moral and financial support throughout my years of education.

Dedication

To my parents

Chapter 1: Introduction

1.1 Basic of Skin Anatomy and Wound Healing

1.1.1 Basic Skin Structure

The skin is the largest single organ of the body, whose functions fall into several broad categories, including protection, sensation, thermoregulation, metabolism, and sexual signaling. Figure 1.1 shows the basic structure of human skin. The skin is composed of the epidermis, a stratified squamous keratinized epithelial layer of ectodermal origin, and the dermis, a layer of mesodermal connective tissue. The epidermis can be divided into five layers. The topmost layer is the stratum corneum (SC), it is consisted of 15-20 layers of flattened cells with no nuclei or cell organelles. Keratin is a family of fibrous structural protein that make up most of the cell content in the stratum corneum. It functions to prevent water loss and protect the body from environmental stimuli. Beneath the SC, there are stratum lucidum (SL), stratum granulosum (SG), and stratum spinosum (SS). These layers contain living keratinocytes originated from the stratum basale (SB), the bottom most layer of epidermis. The SB is a single layer of columnar cells on the basement membrane that separate the epidermis and dermis.. As new keratinocytes are formed, old cells move upward and start to differentiate. During differentiation, these keratinocytes increase the amount of keratin filaments and lose their nuclei and organelles until they reach the SC.. Depending on age, the region of the body, and other factors, the human epidermis is renewed about every 15-30 days. Moreover, there are also three less abundant epidermal cell types in the epidermis: melanocytes, which produce melanin to protect underlying tissues from ultraviolet (UV) damage, Langerhans cells, which are antigen-presenting cells that play a role in the immune response, and Merkel cells, which are essential for the tactile sensation.

The dermis is a layer of connective tissue. It is mainly composed of fibroblasts and the extracellular matrix synthesized, which consists of collagen, elastin, and reticular fibers. The dermis contains two sublayers: the thin papillary layer and underlying reticular layer. Both layers contain rich network of blood and lymphatic vessels that provide both nutritive function and thermoregulatory function. In addition to blood and lymphatic network, the dermis is also richly innervated. Sensory afferent nerve fibers form a network in the dermis for the purpose of various sensory detection.

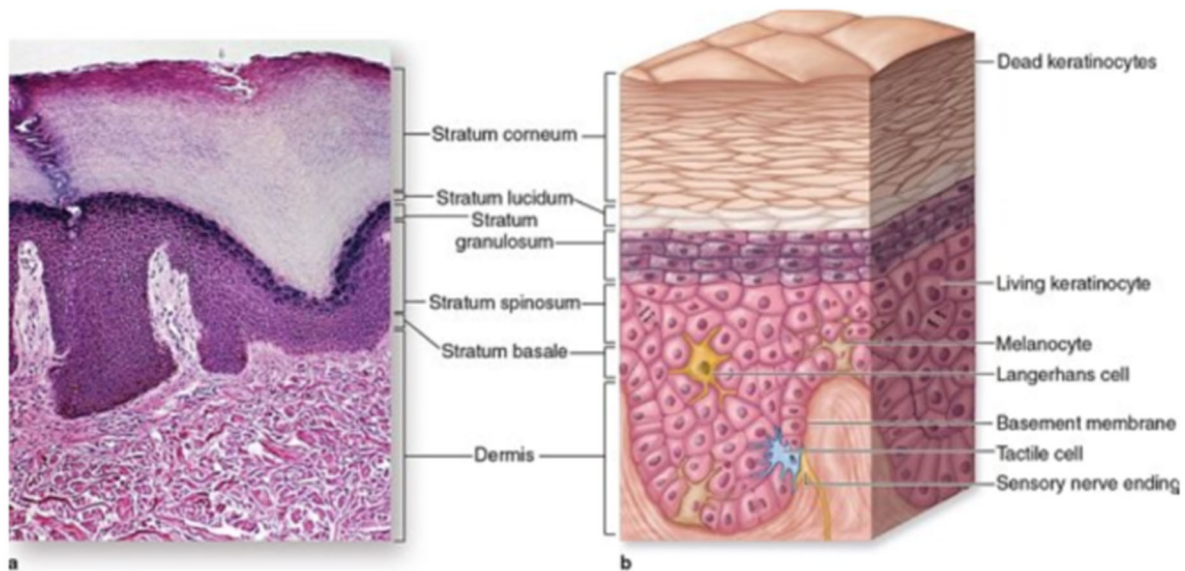


Figure 1. 1 Histology of a skin sample (a) and diagram illustrating the sequence of epidermal layers and different cell types (b). Reproduced with permission from ref. [1].

1.1.2 Wound Healing

As skin serves variety of functions to maintain human well-being, damage to this critical tissue will result in the exposure of the individual to various conditions in the environment, rendering the organism vulnerable to infections, thermal dysregulations, and fluid loss. Thus, it is

critical to maintain integrity of healthy skin, in which wound healing plays an important role. Normal wound healing is a complex and dynamic process that involves the coordination of immune cells, blood cells, various chemical mediators, and extracellular matrix components which all play a critical role in three overlapping phases of the repair process: (1) inflammatory phase; (2) proliferative phase; and (3) remodeling phase.

Inflammatory phase

The inflammatory phase is characterized by a rapid activation of the immune response. Upon exposure of damaged tissue to pathogens, several chemokines and cytokines such as epidermal growth factor (EGF), platelet-derived growth factor (PDGF), and interleukins are being secreted by the platelets and Langerhans cells to attract and activate inflammatory leukocytes to the wounding for purpose of wound decontamination and bacteria destruction. [2-4].

During late inflammation, macrophages produce anti-inflammatory cytokines (IL-10), growth factors (VEGF, TGF- β , and PDGF), and extracellular matrix to lay the foundation of new tissue formation, terminating the inflammatory phase [5, 6].

Proliferative Phase

The proliferative phase is characterized by two major events: the epithelial regeneration and the granulation tissue formation. Partial thickness wound, which involves the epidermis and partially the dermis, heals primarily by re-epithelialization [7]. Keratinocytes would migrate from the wound edge over the denuded area and proliferate to ensure an adequate supply of cells to encase the wound[8, 9]. Full-thickness wounds, which usually involve complete destruction of the epidermis and deep dermis, requires the formation of granulation tissue to replaces the defect

before epithelial covering can occur. During early phase of wound healing, a provisional matrix was laid to act as a scaffold structure for the migration of leukocytes, fibroblasts, and the endothelial cells[10]. After colonize the provisional matrix, fibroblasts start forming granulation tissue by producing collagen and cellular fibronectin-rich matrix [11]. At the meantime, vascularization is also initiated to meet the energy demand of these highly synthetic and proliferative activities [12]. Due to the highly vascularized structure, the wound area appears reddish and is traumatized easily [13]. It is returned to normal state during later remodeling phase.

Remodeling Phase

After the proliferative phase, there is a significant decrease in metabolic needs, this will result in a decrease in angiogenic activity and increase in angiostatic activity, promoting vessel regression[12]. During the remodeling, extracellular remodeling occurs concurrently with vessel regression. Under the influence of cytokines, mechanical stress, and growth factors such as transforming growth factor beta1 (TGF- β 1), many cells of predominantly mesenchymal origin, including the fibroblasts, in the granulation tissue start to differentiate into myofibroblasts, which drive tissue repair by secreting collagen and contracting the extracellular matrix to re-establish tissue integrity and to bring the edges of wound together [10, 14]. After the wound is fully epithelized, myofibroblasts undergo apoptosis through mechanisms that are not yet fully understood[11]. Moreover, through the action of matrix metalloproteinases (MMPs), a family of enzymes that are capable of degrading dermal collagen-rich matrix, the extracellular content is remodeled to be dominated by Type 1 collagen, leading to scar formation which is usually the physiological endpoint of wound repair[15].

1.2 Laser exposure and Non-invasive Measurements

1.2.1 Photothermolysis

In the last decade, the field of laser technology has attracted interest in developing effective and safe skin rejuvenation therapies.. The term photothermolysis referred to the use of light produced by lasers to generate heat damage. Light energy emitted by the laser is absorbed by chromophores in the skin, which then emit the energy to surrounding skin tissue, leading to a thermal destruction[16]. Currently available lasers can be separated into two categories: ablative photothermolysis and non-ablative selective photothermolysis.

Ablative Photothermolysis

Ablative lasers have long been used to treat photodamaged skin. The most commonly used ablative lasers are CO₂ laser (10,600 nm) and Erbium:YAG (2940 nm), which both are strongly absorbed by tissue water, resulting in rapid tissue vaporization, removing the epidermis and upper layers of the dermis in a continuous fashion[17]. This process leads to wound healing with regeneration of the epidermis and remodeling of the dermis. These lasers are effective in improving photodamaged skin, hypertrophic scarring, actinic keratoses, and facial wrinkles, However, ablative photothermolysis is limited to prolonged downtime and significant adverse side effects [18]. To reduce the side effect of this treatment, Manstein et al. [19] first introduced the approach called fractional photothermolysis in 2004. The mechanism with photothermolysis is to destroy a fraction of the skin, creating microscopic cylindrical zones of necrosis. These thermally altered zones are termed Microscopic Treatment Zones (MTZs). The surrounding tissue is spared from the thermal damage, decreasing the amount of epidermal injury and therefore results in rapid re-epithelialization[20]. By carefully selecting the treatment parameters (i.e. energy delivered per

MTZ and density of the MTZ per square centimeter) and number of treatment sessions, fractional photothermolysis can achieve similar outcomes compared to ablative laser therapy with less side effects [17, 21].

Non-ablative Photothermolysis

Selective photothermolysis is a non-invasive laser treatment. This technique is based on the principles of interaction between light and different targets of skin tissue. By selecting different wavelengths that targets specific skin chromophores (hemoglobin, melanin, and external chromophores), the light energy is absorbed only by these specific targets[22]. The absorbed energy will then produce a photothermal reaction that leads to chromophore destruction and formation of heat which ultimately damage the targeted tissue[23]. Studies have revealed improvement of skin conditions such as acne, port wine stain, photodamaged skin, with selective photothermolysis[24-26]. Despite decreased severity and duration of treatment related side effects, the efficacy of this approach is not comparable to those of the ablative lasers for treatment of skin conditions like scarring or significant facial aging. In addition, in situations where the differential absorption between the target and the surrounding tissue was not sufficient, collateral damage may occur due to indiscriminate and nonspecific tissue heating, resulting in damage to normal healthy skin tissue which would lead to unnecessary side effects [27, 28].

Multiphoton-thermolysis

Recently our lab introduced a novel technique called multiphoton-thermolysis, which is based on the concept of multiphoton absorption [29] . A tunable femtosecond Ti:sapphire laser beam with near-infrared (NIR) wavelength was tightly focused on the sample tissue, as single

photon absorption is low within this optical window wavelength range, the radiant energy was directed spatially to the target of interest by aiming the laser focal point at the specific location (Figure 1.2). Sufficient photon density for multiphoton absorption to occur is only achieved at the focal point, whereas no absorption will be generated outside the focal point since the photon density is low. As a result, this novel multiphoton-thermolysis can confer high precision in both horizontal and vertical direction when targeting a specific micro-site for treatment, leaving the tissue above and below the target intact avoiding any unnecessary adverse effects. In other studies that investigate wound healing response, targeted tissue was evaporated by fractional photothermolysis, or physically removed using biopsy. In contrast, in our previous study, after laser exposure, the targeted tissue was left in the region of interest and the surface of the skin was unaffected. This will allow us to investigate any tissue alteration that happened during the laser exposure and observe the following skin dynamics to repair the altered structure.

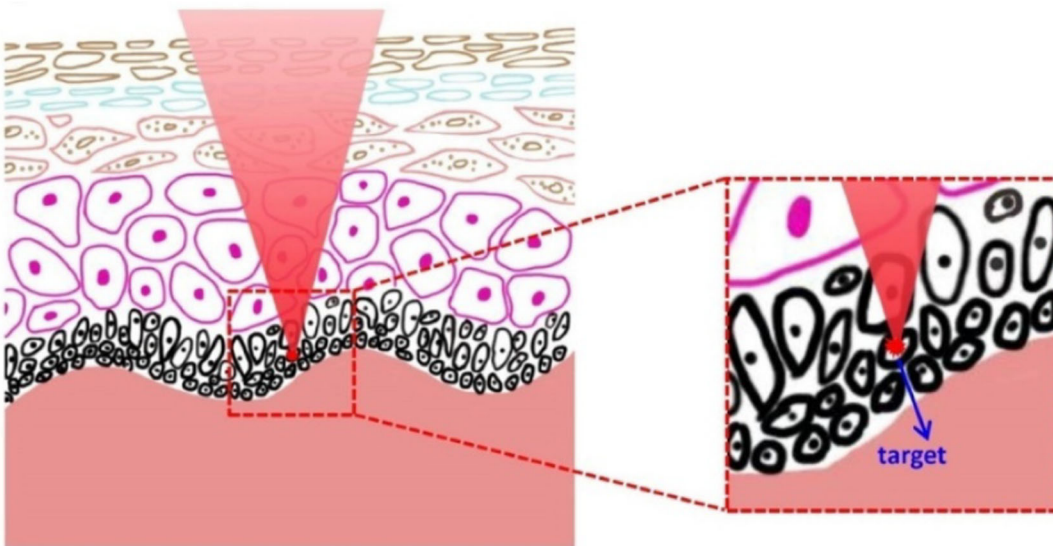


Figure 1.2 Schematics showing the concept of spatially selective photothermolysis. Multiphoton absorption only occurs at the focal point, as the photon density outside the focal point is low.

Reproduced with permission from ref. [29].

1.2.2 Optical Imaging Techniques

Skin abnormalities usually involved multiple layers of skin tissue, which is difficult to examine with naked eye. Histological analysis has long been the gold standard method for diagnosis of skin lesions. Due to its invasive and time-consuming nature, this approach is considered unacceptable for many patients, and researchers have been interested in developing non-invasive approaches for skin diagnosis. Dermoscopy is the examination of the skin surface using optical magnification. It is performed with a handheld instrument called a dermatoscope. This technique is used to help diagnosing skin neoplasms [30]. However, the disadvantage of this technique is that it cannot differentiate signals emitted from different depth of the skin. High frequency ultrasonography is another popular technique used in dermatology. It is based on the phenomenon of transonic wave reflection to generate gray scale images for interpretation[31]. This technique can provide critical depth information that cannot be assessed clinically. However, studies reported that it is an operator sensitive, the accuracy of diagnosis depends on the examiner's level of training [30, 32]. Optical coherence tomography (OCT) is another imaging technique used for skin condition diagnosis. It is based on interference between signal from an object under investigation and a local reference signal. The OCT generates a real time cross-section image of the object, showing different layers of structure of many biological tissues[33]. Although OCT can provide deeper skin tissue imaging, typical OCT systems have a resolution of 5-20 μm , which is insufficient for visualizing cellular morphological changes[34].

In order to achieve better imaging quality and to improve the accuracy of diagnosis of skin conditions, multimodality imaging systems which can provide complementary signals are developed to provide 3D structural and functional information about biological tissues. These

techniques include confocal microscopy, multiphoton microscopy, and image-guided micro-Raman spectroscopy.

1.2.2.1 Reflectance Confocal Microscopy

Reflectance Confocal Microscopy (RCM) is a non-invasive optical imaging technique that uses point illumination and a pinhole in front of the detector to achieve high optical resolution. Figure 1.3 illustrates a sample schematic of the setup of reflectance confocal microscope. As a coherent light was emitted from the laser source, it passes through a light source pinhole which will make the laser beam become a point light source. The point source light is then reflected by a beam splitter and focused onto a small spot (micron size in diameter) on the specimen by an objective. Reflection occurs at the boundary of two cellular structures or organelles that have different refractive index. Reflected light from the focal point propagates back to the objective lens and was focused into another small pinhole positioned in front of the photodetector. This pinhole has a diameter of its aperture that matches that of the illuminated spot. The fact that the point source light, the spot being illuminated in the sample, and the pinhole aperture lie on the optically conjugate focal planes, is where the name “confocal” was originated[35]. As a result, light returning from above or below the focal point is masked out by the pinhole, so that the photodetector only receives signal generated from the point that we are interested. By scanning horizontally in x-axis and y-axis direction (parallel to the plane of focus), and by changing the depth at which the objective lens focuses in the vertical direction, information about any particular layer within the specimen can be acquired. Then images from different layer can be constructed vertically to generate a 3D structure of the tissue. The imaging depth of this technique in tissue is about 200 μm , making it an ideal option for skin analysis. It allows in vivo microscopic analysis

of skin lesions at a level of resolution close to histological details [36]. For example, the early detection of malignant melanoma is critical, as melanoma is usually curable by complete excision at early stage. RCM represents a novel imaging modality particularly suitable for examination of pigmented lesions. Since melanin is an effective scatter, they appear as white bright image signal under the RCM and can act as a cytoplasmic contrast-providing agent for in vivo analysis and identification of melanocytes and their distribution within the epidermis[37]. Studies have showed that RCM is able to detect melanoma based on established criteria of histopathological analysis including pagetoid spread of melanocytes, predominance of single cells over nests, presence of enlarged melanocytes, and irregular intraepidermal growth of melanocytes at the periphery of lesions[38, 39]. Overall, a sensitivity of 88.15% and a specificity of 97.6% were achieved when evaluating the diagnostic applicability of RCM in melanoma[40].

However, as RCM is based on reflection of light from various cellular structures that have different refractive index, it can only provide morphological information of tissue. The biochemical composition or the identification of specific molecules cannot be analysis using this imaging modality.

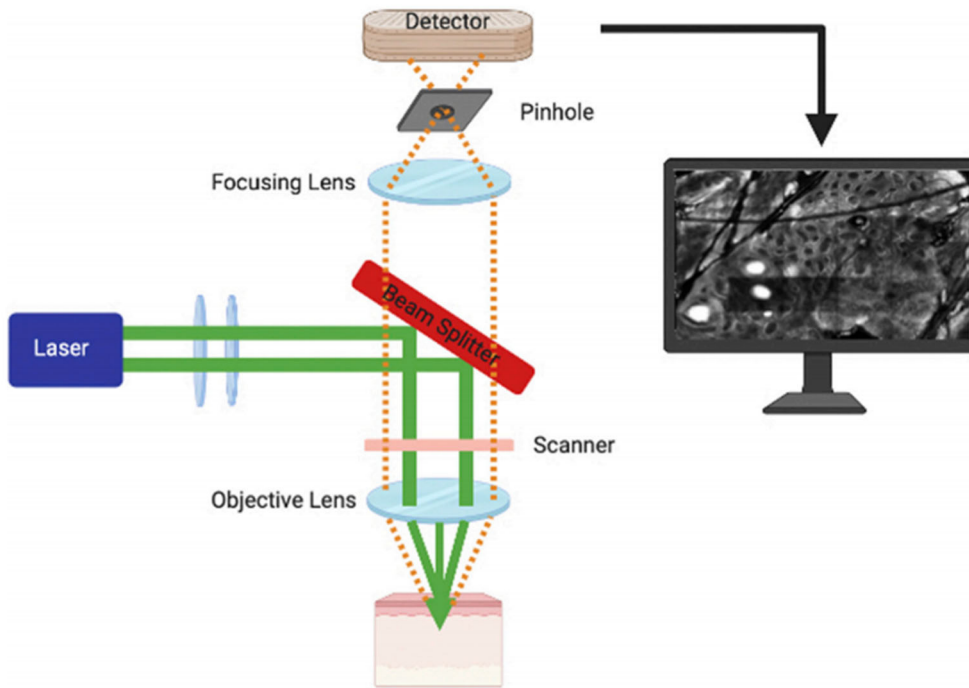


Figure 1.3 Schematic picture of basic set up of reflectance confocal microscope. Incident light is shown in green solid line, and the reflected light from the sample is shown in orange dash line. Reproduced with permission from ref.[36].

1.2.2.2 Two-Photon Excitation Microscopy

Two-photon excitation fluorescence (TPEF) microscopy is a fluorescence imaging technique which employs the process called two-photon absorption. Figure 1.4 illustrated the difference of single-photon fluorescence and two photon fluorescence. There are many naturally presented fluorophores in human skin, such as reduced nicotinamide adenine dinucleotide (NADH) and flavin adenine dinucleotide (FAD), and melanin[41]. In conventional one-photon fluorescence, these fluorophores absorbed the energy from an incident photon, and enters its excited state. When they return to a lower energy state, the absorbed energy is now released through the emission of a fluorescence photon. The emitted light has a longer wavelength (lower

energy) than the absorbed incident light. In contrast, in TPEF, two low-energy photons were absorbed by the same fluorophore at the same time to excite the fluorophore into a higher energy state. The emitted light has a shorter wavelength than both incident photons. Two-photon excitation is a nonlinear process with the absorption rate depends on the second power of the excitation light intensity. And as the distance move away from the vicinity of the focal point of the laser, the light intensity drops quadratically[42]. As a result, this two-photon excitation occurs almost exclusively at the focal point. Photodamage refers to photobleaching (the gradual decline in the fluorophore's ability to fluoresce) and phototoxicity (the toxic effect of activated fluorophores on cells). Each excitation event carries the risk of photodamage. Since two-photon excitation only occurs at the focal point, TPEF can drastically reduce these unwanted side effects. In addition, TPEF usually use near-infrared light as the excitation light source, which can minimize the scatter event happen in the tissue, significantly increase the penetration depth compare to single photon excitation[43].

In cells, the TPEF signal is mainly derived from NADH and FAD of the cytoplasm[44], making it a great tool to visualize cellular tissue architecture and cell morphology with detailed resolution comparable to HE sections[45]. As a result, researchers have tried to investigate the potential in the early detection of cancerous tissue [46-48]. In a systematic review paper that analyzed the general detection of tumor without further differentiation with 440 samples, an overall sensitivity of 94%, specificity of 96%, and 95% accuracy for detection of malignant tissue was achieved using TPEF images[43]. However, cell nuclei are not visualized directly by TPEF, but are detected as an area with absence of TPEF signal[49]. Therefore, histological analysis is still considered to be more accurate for visualization of some important cancer characteristics such as chromatin condensation, mitosis, and apoptosis of cells [50].

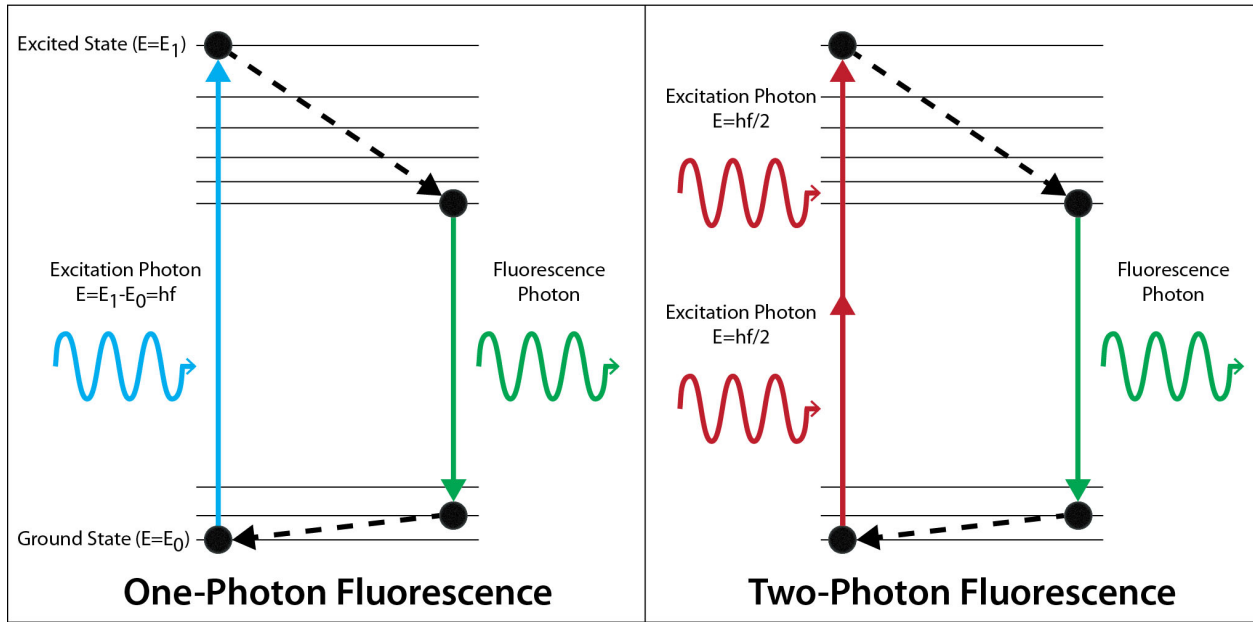


Figure 1. 4 Schematic drawing illustrating the processes of fluorescence: (left) single-photon fluorescence (right) two-photon fluorescence.

Image source: <https://psychology.stackexchange.com/questions/13829/voltage-sensitive-dyes-technique-2-photons-microscopy-vs-confocal-microscopy>

1.2.2.3 Second Harmonic Generation Microscopy

Second harmonic generation (SHG) is also a nonlinear optical process. Unlike TPEF, in which two photons are absorbed by the target to produce a single photon with some energy loss, whereas SHG signal has no absorption events occurred. SHG signal involves scattering events whereby two photons interacting simultaneously with a non-centrosymmetric target molecule combine to produce a new photon with exactly twice the frequency and half the wavelength[51]. Figure 1.5 illustrated the difference in TPEF and SHG. SHG has been widely used as a quantitative modality for imaging non-centrosymmetric proteins such as collagen in a diverse range of tissues[52]. As collagen is the most abundant non-centrosymmetric protein in vertebrates, it forms

the structural network of the extracellular matrix (ECM), SHG is highly sensitive to diseases that lead to collagen-associated changes, such as cancer, fibrosis, and connective tissue disorders. For example, quantitative analysis of the ratio of forward and backward propagating SHG signal (F/B ratio) revealed that this ratio underwent significant evolution during breast cancer progression[53].

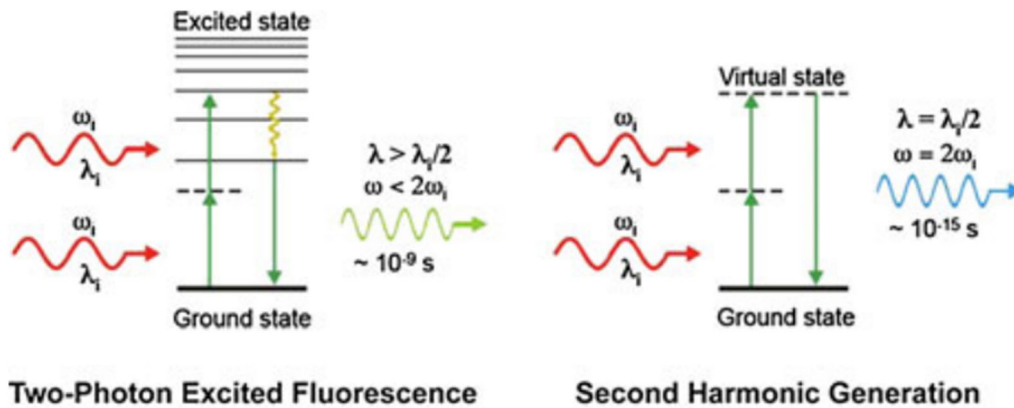


Figure 1.5 Comparison of TPEF and SHG. In TPEF. Two incident photons are absorbed simultaneously to excite the molecule to a higher energy state, and the emission of a single photon happened when the molecule return to its ground state. The emitted photon has wavelength greater than half of the incident photon. Whereas in SHG no absorption events happens, there is no energy loss during the interaction of incident photons with the molecule, resulting in a emission of photon with exactly twice the frequency and half the wavelength. Reproduced with permission from ref.[51].

1.2.2.4 Raman Spectroscopy

Raman spectroscopy is a spectroscopic technique that detects inelastically scattered photons from molecules to provide its chemical and structural information. When a source of monochromatic light, usually from a laser, interacts with a molecule, the majority of the photons undergoes Rayleigh/elastic scattering, where there are no energy changes. However, a small

fraction of the photons can gain or loss energy from interacting with the vibrations of a molecule. This process is called inelastic scattering, also known as “Raman scattering”[54]. When the incident photon loss energy to the vibration, a process termed “Stoke Raman Scattering”, the scattered photon will have lower energy and longer wavelength (Red Shift); if the incident photon gain energy from the vibration, this is termed “anti-Stokes Raman Scattering”, the scattered photon will have higher energy and shorter wavelength (Blue Shift). Due to this difference in the wavelength and energy between the incident and scattered photon, the elastic scattering can be filtered out and the rest of the Raman scattering signals can be collected and dispersed onto a detector [55]. Within a molecule, each chemical bond vibrates at different frequency that will produces different Raman signal. The Raman spectrum is generated by plotting the intensity of Raman signal against these frequencies (as Raman shift in cm^{-1}). This will allow a unique spectrum to be generated for each molecule and can act as a fingerprint for biochemical identification within a tissue or sample[56]. Because Raman spectroscopy can provide this relatively detail information about the biochemical composition of the sample, changes that occur in the tissue during disease progression can be detect, and thus, this technique can be a potentially universal method for disease diagnosis including cancers[57].

In our lab, we developed a system called “Imaging-guided Micro-Raman spectroscopy (IMRS)”, that allows the simultaneous acquisition of video-rate imaging and Raman signals. This system has two major benefits compare to conventional Raman measurement. First, the field of view of the imaging system can range from $20\ \mu\text{m} \times 20\ \mu\text{m}$ to $200\ \mu\text{m} \times 200\ \mu\text{m}$, this will allow us to measure the Raman signal within these microscopic area. Second, the imaging system will facilitate the localization to the exact same microscopic site that can guarantee the monitoring of the Raman changes in the region of interest over a long period of time. In this study, the

multimodality microscope was built by incorporating the IMRS with the multiphoton microscope (MPM). Comprehensive information can be acquired by this new modality, since the TPF and SHG signals from the multiphoton microscope and can provide us with detailed cellular morphology characteristics and tissue structural modifications, and the IMRS will allow the identification of any biochemical changes.

1.2.2.5 Optical Redox Ratio

Skin tissue contains many naturally existed fluorophores that can be efficiently excited and imaged using MPM. Among these fluorophores, nicotinamide adenine dinucleotide (NADH) and flavin adenine dinucleotide (FAD) are of particular interest, because these cofactors are involved in metabolism and can reflect the metabolic state of the tissue being studied [58]. During oxidative phosphorylation, the primary redox reaction in cells to generate energy, NAD^+ is reduced to NADH, and FAD is oxidized to FADH_2 . Since only NADH and FAD are both fluorescent during these processes, and have different excitation and emission maxima wavelengths, their abundance can be represented by their fluorescence intensities with the implement of proper excitation wavelength and emission filters. The ratio of these measured fluorescence intensities of NADH and FAD can then be used to determine the optical redox ratio based on the equation $FAD/(NADH + FAD)$ [59]. A higher optical redox corresponds to a lower metabolism, and lower optical redox ratio is corresponded to a higher metabolism. Since the real-time measurements of the intensities of NADH and FAD are noninvasive using MPM, this technique is capable of providing longitudinal and quantitative assessments of keratinocyte cell metabolism, which could serve as an effective biomarker for wound healing related studies. In this study, we are investigating the skin's dynamic response after the laser exposure, we would expect the redox ratio

to be reduced since cells at the basal layer will increase their proliferation and differentiation activities to compensate for the loss of cells during laser exposure. In addition, cancer cells often have very high metabolism to meet the energy demand during intensive proliferation, and optical redox ratio displays the metabolic rate in a more straight forward way, and thus it has a great potential in the application in cancer research including cancer diagnosis and prognosis, cancer subtype identification, and monitoring therapeutic effects [60-62].

1.3 Objective and Hypothesis

To improve the precision and efficiency of currently available laser therapies, we developed multiphoton-thermolysis based on the concept of multiphoton absorption. One of the major goals of this study is to evaluate the capability of multiphoton-thermolysis to induce *in vivo* photothermal alteration in normal human skin. I hypothesize that this technique is able to generate sufficient and precise tissue alterations, and to initiate wound-healing like responses including inflammation and tissue remodeling, which may be potentially used in future treatment of various skin conditions that require precise targeting of specific skin components.

In addition, to improve currently available technologies on disease diagnosis and treatment prognosis, it is important to acquire complementary and real-time information from the tissue being studied, as each of the above-mentioned individual modalities provide limited messages. One of the major goals of this study is to test the ability of our multimodal microscopy to detect skin alterations and to monitor skin dynamics after a laser exposure. I hypothesize that 1) tissue architectural modifications and cellular morphological and metabolic changes after the induction of photothermal alterations can be captured by the MPM imaging system; 2) biochemical changes during tissue recovery can be identified by the IMRS system.

Chapter 2: Materials and Methods

2.1 Study Design

To study the *in vivo* skin dynamics after multiphoton-thermolysis laser exposure, this pilot study recruited 5 volunteers (Fitzpatrick skin type II). For each volunteer, two different sites on the inner forearm were selected and imaged, each site corresponding to different target skin layer for the laser exposure: epidermis, and dermis. The skin dynamics to the laser exposure was imaged with MPM and IMRS at seven time points after the laser exposure: immediately after, 3 hours, 24 hours, 3 days, 1 week, 2 weeks, and 4 weeks. The multiphoton-thermolysis and all *in vivo* measurements were approved by the University of British Columbia Clinical Research Ethics Board (Certificate #: H19-02318), and all experiments were conducted with written informed consent obtained from each volunteer.

Multiphoton Microscopy

In this study, we used a prototype real-time MPM imaging system that was developed in our lab[29] for *in vivo* measurements of volunteers' skin (Figure 2.1 1). The system used a tunable femtosecond Ti: sapphire laser (720-960 nm, 80 Hz, 150 fs) and had two photomultiplier tube (PMT) detectors for TPF and SHG signals, respectively, plus one avalanche photodiode (APD) for simultaneous acquisition of the RCM signals (fsRCM). The image field of view (FOV) was set at $200\ \mu\text{m} \times 200\ \mu\text{m}$, and the laser power was set at 40 mW. Each imaged site was measured four times with four different excitation wavelengths and filters combinations to achieve optimal visualization of different components within the skin: 1) 750 nm excitation wavelength with a band-pass filter centered at $460 \pm 20\ \text{nm}$, for NADH imaging; 2) 750 nm excitation with no filter for cell shape and morphology visualization; 3) 810 nm excitation wavelength with a $390 \pm 20\ \text{nm}$

bandpass filter for collagen structure visualization; and 4) 900 nm excitation wavelength with a band-pass filter centered at 525 ± 20 nm for FAD imaging. For each excitation wavelength and filter combination, 3D images were acquired by stacking the horizontal images (x-y) collected at different depth from the skin surface to the bottom. This was achieved by moving the objective along the Z direction through the piezoelectric scanner. Each step of the z scan was 1 μm , and a total depth of 150 μm was imaged for each measurement. The 3D image ($200 \mu\text{m} \times 200 \mu\text{m} \times 150 \mu\text{m}$) was reconstructed using the software Image J (Image J 1.53e, National Institutes of Health).

Multiphoton-thermolysis laser exposure

For each volunteer, two separate microscopic locations were selected to receive the multiphoton-thermolysis laser exposure. One site was located 30 μm underneath the skin surface for epidermal skin alteration, the other site at a different location was selected at 50 μm underneath the skin surface for dermal alterations. The exposure FOV was set at $50 \mu\text{m} \times 50 \mu\text{m}$ for the epidermis and $20 \mu\text{m} \times 20 \mu\text{m}$ for the dermis. Laser power was increased to 200 mW to induce photothermal skin alteration. The exposure time was controlled by a programmable shutter and set at 4s.

Image-guided Micro-Raman Spectroscopy

A CW-laser with a 785 nm wavelength was used to excite Raman signals in the laser exposure area and to acquire RCM images (cwRCM). The cwRCM imaging was used to identify the target of interest and to guide where micro-Raman is acquired. The FOV was $200 \mu\text{m} \times 200 \mu\text{m}$. After correctly located to the laser exposed site, the FOV was reduced to $50 \mu\text{m} \times 50 \mu\text{m}$ for the epidermis or $20 \mu\text{m} \times 20 \mu\text{m}$ for the dermis to measure the Raman signal, which was collected

by a liquid nitrogen-cooled, back-illuminated deep depletion CCD. Each Raman spectra was measured repeatedly for 3 times. Their intensity was first calibrated using a Standard Reference Material 2241 (National Institutes of Standards and Technology, U.S.), and was then further analyzed according to Vancouver Raman Algorithm (VRA)[63]. The final Raman spectra for the laser exposure site was calculated by taking average of the processed Raman data.

2.2 System setup

This thesis used a multimodality microscopy system that incorporated a MPM and an IMRS. The MPM system was configured to acquire TPF, SHG, as well as RCM images and to generate micro-alteration using multiphoton-thermolysis in volunteer's skin. And the IMRS system was used to measure the Raman signals of the interested site guided by RCM images. Figure 2.1 presents the schematic drawing of the multimodality microscope.

Multiphoton Microscope

For multiphoton microscopic imaging, a tunable femtosecond (fs) Ti:Sapphire laser beam (720-960 nm, 80 MHz, 150 fs) passes through a motorized half wave plate (HWP) and a polarization beam splitter (PBS1) which were used to adjust the laser power. Then the beam was directed to a prism pair system for pulse width compensation (Figure 2.1, red dashed line). The D-shaped mirror will allow the laser beam from the laser source to pass through, and will re-direct the beam coming back from the prism system to a lens pair (L1 and L2), to expand the laser beam size to 4 mm. The laser was then directed through the laser shutter and a quarter wave plate (QWP) to a x-y scanner (composed of two scanning mirrors) and was then focused onto the volunteer's skin by a 60X water-immersion microscope objective (LUMPLFLN60X/W,

Olympus Canada, Markham, Ontario). TPF and SHG signals from the volunteer's skin were collected by the objective and directed to their respective photomultiplier (PMT) (H9433MOD-03, Hamamatsu Corp., Bridgewater, New Jersey) through a dichroic mirror (Figure 2.1, green line). Before the signals enter their respective PMTs, they first pass through a filter cage (Figure 2.1, blue cube). The filter cage is composed of a dichroic mirror and two filters located at the exit side of the cage. For cellular morphology and dermal structure visualization, 750nm and 810 nm excitation wavelengths were used, and the filter cage only contains a dichroic mirror separating at 405 nm. As a result, the TPF signal from cellular component of the skin will be directed to the TPF PMT1, and SHG will be directed to the SHG PMT. To measure the intensity of NADH and FAD, another filter cage that is composed of a 495 nm dichroic mirror (Semrock, FF495-Di03) there are two band pass filters centered at 447 nm (Semrock, FF02-447/60-25) and 525 nm (Semrock, FF03-525/50-25), so that when excited at 750 nm, the NADH signal can be collected from the SHG PMT, and the FAD signal can be collected at the TPF PMT when excited with 900 nm. And the fs-RCM signal was collected by the same objective, passed through the quarter-wave plate, and then redirected by PBS2 to another lens (L8), which will focus the signal into an avalanche photodiode (APD) (C10508, Hamamatsu Corp., Bridgewater, NJ) with a pinhole located in the front for confocal imaging.

For multiphoton-thermolysis, the same light path was used as in the microscopic imaging system. However, in order to generate the laser alteration, we have to increase the laser power to 200 mW. Since, the laser loses a substantial amount of energy in the prism system, we had to bypass the prism system by inserting a flip mirror (Flip Mirror 1) in front of the D-shaped mirror. When this mirror was flipped up, the light was directly reflected and directed to the x-y

scanner without entering the prism system. In addition, a programmable shutter was placed before the scanner to control the duration of laser exposure.

Image-Guided Micro-Raman Spectroscopy

A continuous-wave (CW) laser at 785 nm was used for measuring the micro-Raman signal (Figure 2.1, orange line). A half wave plate (HWP) located at the laser exit port was used to control the laser power. Another flip mirror (Flip Mirror 3) was placed in front of the laser shutter. When the mirror was up, the CW laser beam was directed to the scanner and focused on the volunteer's skin using the same light path as the *fs* laser, while the *fs* laser was blocked by the flip mirror. This set up allowed us to switch between the MPM system and the IMRS system. The Raman signal from the sample was collected by the microscope objective, directed through the QWP to a short pass (SP) filter. As the Raman signal has a longer wavelength, it is then reflected by the SP to an optical fiber, which has a diameter of 50 μm and acts as a pinhole for confocal Raman detection. While the shorter wavelength cw-RCM signal passed through the SP it was directed to the APD by PBS3 to achieve the simultaneous acquisition of images and Raman signals.

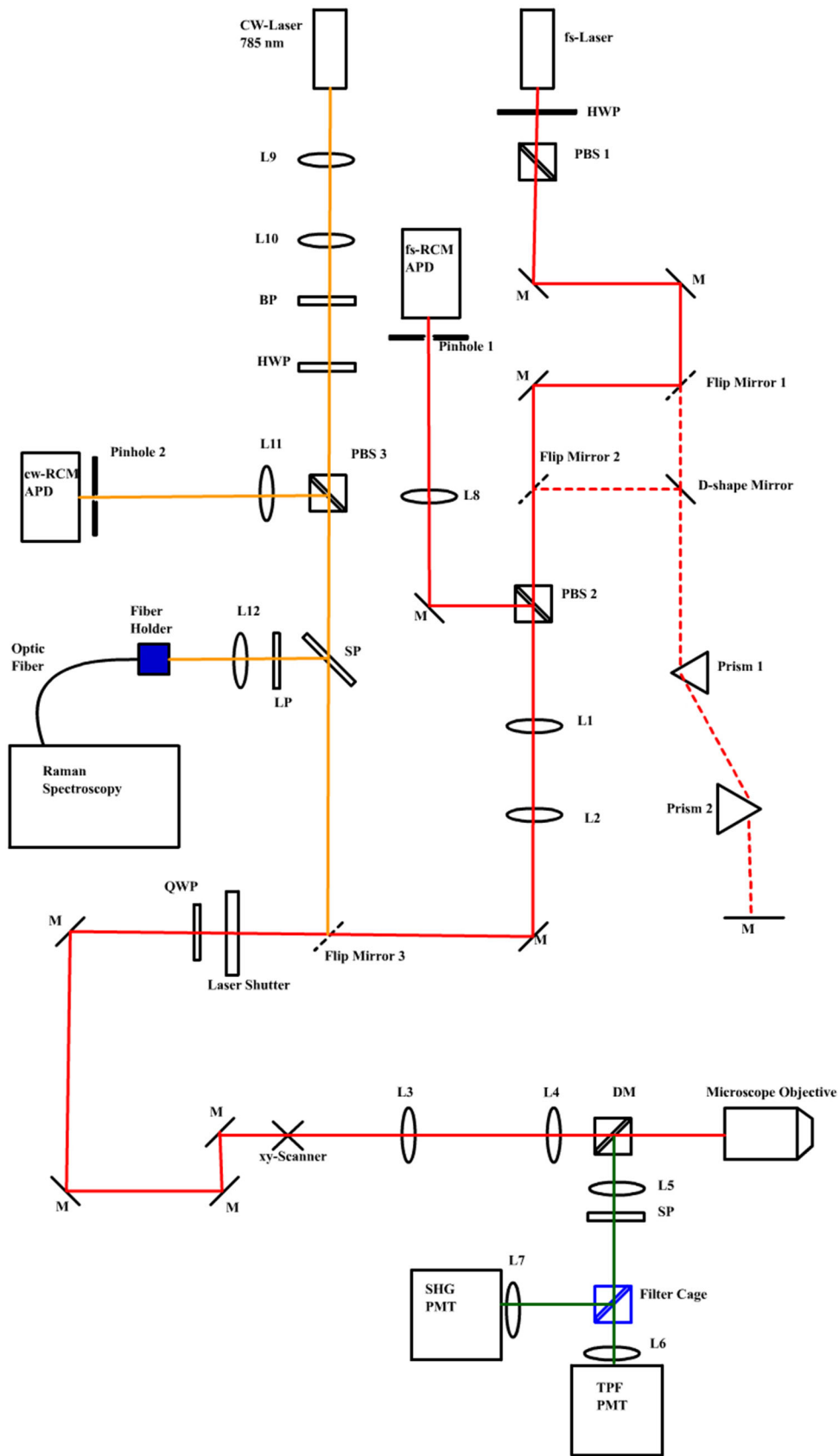


Figure 2. 1 System diagram of the in vivo multimodal microscopy that incorporated the IMRS (orange) and MPM (red) system. HWP: half wave plate; QWP: quarter wave plate; DM: Dichroic mirror; PBS: polarization beam splitter; M: Mirror; APD: avalanche photodiode; L: lens; LP: long pass filter; SP: short-pass filter; PMT: photon multiplier tube

Clinical Volunteer Measurements

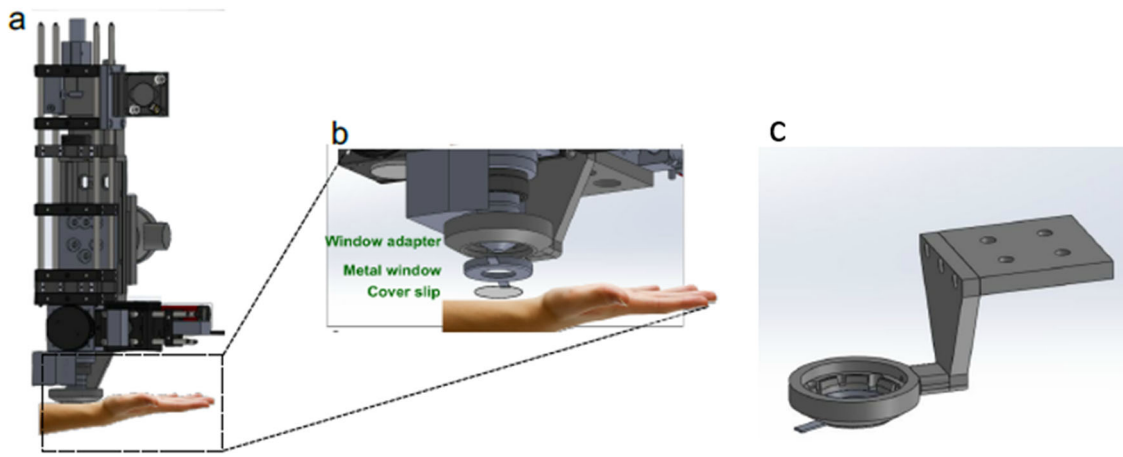


Figure 2. 2 Clinical measurement set up of the imaging head. a). configuration of the imaging head; b). illustration of the imaging head and subject skin interface; c). metal window anchored to the window adapter.

Clinical measurement of volunteers was realized by a special design of the imaging head. The imaging head was composed of the scanning unit, scanning lens, relay lens, objective, PMTs, and translational stages and z stage (Figure 2.2 a). A L shaped window adapter (Figure 2.2 c) was secured to the bottom of the xyz translational stage. A skin measurement window with an 18 mm diameter opening can be anchored on this window adapter. Before each measurement, a coverslip (Electron Microscopy Sciences, Cat. # 72256-06) was attached to the window on one

side and attached to the skin on the other side with adhesive tape (Figure 2. 2 b). The measurement window and the coverslip, together with the skin, were then anchored on to the window adaptor. Water was added between the objective and the coverslip, as well as between the coverslip and the skin surface to match the refractive index. After each imaging session, the measurement window and the coverslip could be detached from the window adapter and subject's skin. The coverslip was discarded and replaced after each use.

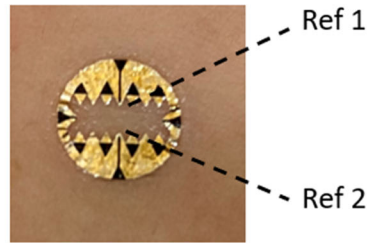
2.3 Re-localization

The precise relocalization to the same microscopic laser exposed site on *in vivo* human skin at successive time points was achieved by the application of a custom designed temporary surface marker [64]. An FDA-approved metallic temporary surface marker decal was designed to be about 10 mm diameter circular shape with a $2.5 \times 8 \text{ mm}^2$ rectangular center opening (Figure 2.3 a). The edge of the rectangular opening was designed to be serrated so that the tips can be used as coordination markers to facilitate the relocalization. This temporary surface marker decal was applied before the first measurement and remained intact on the skin for up to 2 weeks. For the purpose of this study, we needed to monitor the skin response for 4 weeks. So, at the beginning of the 2-week measurement, a larger marker (outer diameter: 15 mm, inner diameter: 12 mm) made with the same material was applied to encircle the smaller marker (Figure 2.3 c). The tips of the new larger marker were then used as new reference coordination points for precise relocalization.

a. Surface marker design



b. Surface marker on skin



c. Larger surface marker

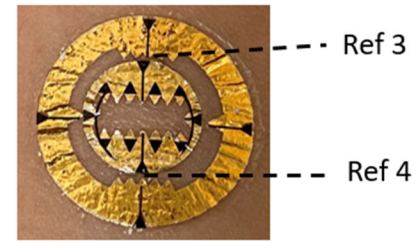


Figure 2. 3 Surface marker design. (a) illustration of surface marker design. Diameter: 10 mm, center rectangular opening: $2.5 \times 8 \text{ mm}^2$. (b) White light image of surface marker decal on skin. The central tips are used as the reference points (Ref 1 and Ref 2) (c) Larger surface marker encircling the smaller marker. The tips of the larger marker were now used as the new reference points (Ref 3 and Ref 4).

Procedure for relocalization using the surface marker:

1. Prior to imaging, the surface marker was applied onto the volunteer's skin.
2. At the baseline imaging session, two reference tips (Ref 1 and Ref 2) were selected and imaged using both a white light camera and RCM; the xy coordinates of the two reference points were recorded and denoted as (x_1, y_1) and (x_2, y_2) by controlling the motorized translational stage.
3. The center point between the two reference tips at the baseline imaging can be calculated and localized as $(x_3 = \frac{x_1+x_2}{2}, y_3 = \frac{y_1+y_2}{2})$. After finding the center point, the target site for laser exposure can be selected using the MPM system. And the coordinates of the target site can be recorded as (x_4, y_4) .
4. The distance between the laser exposure site and the center points can be calculated as $(\Delta x = x_4 - x_3, \Delta y = y_4 - y_3)$

5. At each of the follow up imaging sessions, the coordinates of the two reference points were recorded using the same method as described in the second step. And the new center point was calculated and localized as (x'_3, y'_3) . Then the laser-exposed site can be found using the new coordinates $(x = x'_3 + \Delta x, y = y'_3 + \Delta y)$.
6. Adjust the z stage to image the relocated site to compare the biological structures (including skin creases, vessel features, collagen structures) with the baseline images. And fine adjust the xy stage until the FOV is the same as that of baseline.
7. At week two, the larger surface marker was applied to the skin of the volunteer before the measurements were taken, the black lines on reference points 3 and 4 (Ref 3 and Ref 4, Figure 2.3) of the larger marker were aligned with the black lines on Ref 1 and Ref 2 of the smaller marker.
8. The laser exposure site was located using Ref 1 and Ref 2 as described above, then Ref 3 and Ref 4 of the larger marker was located with the assistance of white light camera. Their coordinates were recorded as (x_{L1}, y_{L1}) and (x_{L2}, y_{L2}) .
9. The new center point (x_{L3}, y_{L3}) and its distance to the laser exposure site $(\Delta x_L, \Delta y_L)$ were then found using the same method as described above and were then used for localization of the laser exposure site for further measurements after the two-week time point.

2.4 Optical Redox Ratio

During each measurement session, the laser exposure sites were excited with different wavelengths for NADH and FAD. Their emitted fluorescence signals were then collected by two PMTs with emission filters at 447 ± 30 nm (Semrock, FF02-447/60-25) and 525 ± 25 nm (Semrock, FF03-525/50-25), respectively. At 750 nm excitation, the NADH autofluorescence

was collected with the 447 nm channel; and at 900 nm excitation, the FAD autofluorescence was collected with the 525 nm channel. For each excitation wavelength, a stack of xxx images spanning a 150 μm depth was acquired. To study the metabolic change of the stratum basale in response to multiphoton-thermolysis, the images for both NADH and FAD at the basal layer were extracted. Then the pixels' intensity of these two images were imported into MATLAB to generate two 512×512 matrices. Optical redox ratio (ORR) was computed by pixel-wise calculation according to the equation $[FAD/(NADH + FAD)]$. The average epithelial ORR at the basal layer was calculated from the redox ratio at each pixel at each time point of measurements.

2.5 Measurement Procedure

Procedures for multimodality imaging

1. At the volunteer's first visit, a site of interest was selected with naked eye; major blood vessels, moles, or other skin lesions were avoided.
2. The site of interest was cleaned with 70% isopropyl alcohol wipes and the surface marker was applied to mark the region. Attach the metal skin measurement window to the volunteer's skin with double sided tape, so that the surface marker was centered in the opening of the window. A drop of water was added between the window and the skin.
3. Anchor the measurement window, together with the volunteer's skin on to the window adapter on the imaging head. Add a drop of water on top of the cover glass on the measurement window and lower the imaging head so that the objective just touches the water drop.

4. Then a precise location for the laser exposure was selected, and the coordinates were recorded as previously described in section 2.3.
5. The excitation wavelength for the first measurement was set at 810 nm, and the laser power was set at 40 mW. A dichroic mirror separating at 405 nm was used to segregate the TPF and SHG signals. Set the parameters on the computer software, so that the system will interrogate a volume of the targeted skin region with dimensions of 200 μm (width-x) \times 200 μm (long-y) \times 150 μm (deep-z).
6. Set the step size to 1 μm , so that the system will take an image at each micrometer; the final volume measured will be 150 images stack.
7. Take the volume.
8. Then change the excitation wavelength to 750 nm, for better visualization of the cellular component at the epidermis, and the imaging parameters was the same as above-described steps. Then take another volume.
9. Change the filter to a band pass filter centered at 447 ± 30 nm. This will measure the intensity for NADH. Keep all the laser parameters constant and take another volume.
10. Change the excitation wavelength to 900 nm, and a band pass filter of 525 ± 25 nm was used to replace the 447 nm filter. This will measure the FAD intensity. Take the last volume.
11. Then flip the mirror, which will block the femtosecond laser to let the continuous wave laser to be directed to the targeted region.
12. Use the RCM to confirm the location of the targeted region and measure the micro-Raman signal.

Multiphoton-Thermolysis Laser exposure

- Block both the femtosecond and the continuous wave lasers with a programmable shutter that is controlled by the software.
- Flip down the flap mirror 3 to switch to the femtosecond laser system.
- Flip another set of mirrors as described in section 2.2 to allow the system to bypass the prism pair. Change the excitation wavelength to 780 nm and increase the laser power to 200 mW. And set the exposure time to 4 s.
- Then turn on the shutter, it will automatically shut off after 4 s. and the multiphoton-thermolysis of the targeted region is completed.

2.6 Data analysis and processing

The imaging results were processed with the software Image J. The TPF signal was pseudo-colored as green, and the SHG signal as magenta. The 810 nm excitation wavelength combines the TPF and SHG signal, so that it displays the epidermal and dermal structure simultaneously. The micro-Raman data was processed with the software Origin Lab (Origin Pro 9.8.0.200, OriginLab Corporation), and each Raman spectrum was normalized to the area under the curve. The optical redox ratio was computed using MATLAB (R2020b, Mathworks). The images for both NADH and FAD at the basal layer were extracted. Then, the pixels' intensity of these two images were imported into MATLAB to generate two 512×512 matrices. Optical redox ratios (ORR) were computed by pixel-wise calculation according to the equation $[FAD/(NADH + FAD)]$. The average epithelial ORR at the basal layer was calculated from the redox ratio at each pixel at each time point of measurements.

Chapter 3: Results and Discussion

3.1 Multiphoton Imaging

In this study, we targeted both the epidermis and dermis using multiphoton-thermolysis to generate micro tissue alterations and investigated the subsequent skin response dynamics in five volunteers. In the epidermis, all volunteers displayed immediate responses after the laser exposure; representative images are shown in Figures 3.1- 3.4. However, only one of the five volunteers showed identifiable alterations in the dermis (Figures 3.5- 3.6). These images are pseudo-colored images, with the green color representing TPF signal from cellular components such as NADH and FAD, whereas magenta color represents SHG signal from extracellular dermal collagen.

3.1.1 Epidermis

For this study, we aimed to generate the laser thermolysis at the same depth underneath the skin surface in the epidermis. However, due to the variation in the volunteers' skin thickness, the targeted areas end up in different layers: with two volunteers received the laser thermolysis in the Stratum Basale and three volunteers received the laser exposure in the stratum spinosum. Representative MPM images of the volunteer's epidermis were shown through Figures 3.1 –3.4.

Laser thermolysis in the stratum spinosum

Figure 3.1 Shows the en-face MPM images of the epidermis surrounding the laser exposed area before and at different time points after the laser thermolysis. The laser thermolysis was focused in the stratum spinosum layer. The MPM images acquired before the laser exposure (Figure 3.1 a) show normal morphology and distribution of keratinocytes. The keratinocytes

appear as hollow spherical structure as major MPM signals arise from cytoplasmic content such as NADH, melanin, and FAD, the word “hollow” means that there is no signal generated from the cells nuclei. The volunteers then received the multiphoton-thermolysis and their following skin responses were monitored at 7 time points over a 4-week period (Figure 3.1 b-h). Immediately after the thermolysis, the targeted area showed significant increase in the fluorescence intensity. Exposed cells within the targeted area still maintained their cellular structures but can be distinguished by enlarged nuclei, indicated by white arrows (Figure 3.1 b and c). Starting from day 1 after, more pronounced changes were observed. Individual exposed cells started to lose their morphological characteristics and cellular content started spreading over the neighboring area. Small membrane bounded vesicles can be observed at this time point (yellow arrowhead, Figure 3.1 d). These changes continued to occur until day 3. At this time point, no cellular structures can be identified within the targeted area. At week 1 and later time points, the shape and structure of the targeted area did not display more observable changes, the area was left with content termed as microscopic epidermal necrotic debris (MEND), which was described in previous studies[65, 66]. The MEND was mainly composed of keratinocyte cell fragments and substantial amounts of melanin. This MEND was observed in superficial regions just beneath the stratum corneum at week 1 and continued to migrate upward at later time points, until it was exfoliated from the skin surface.

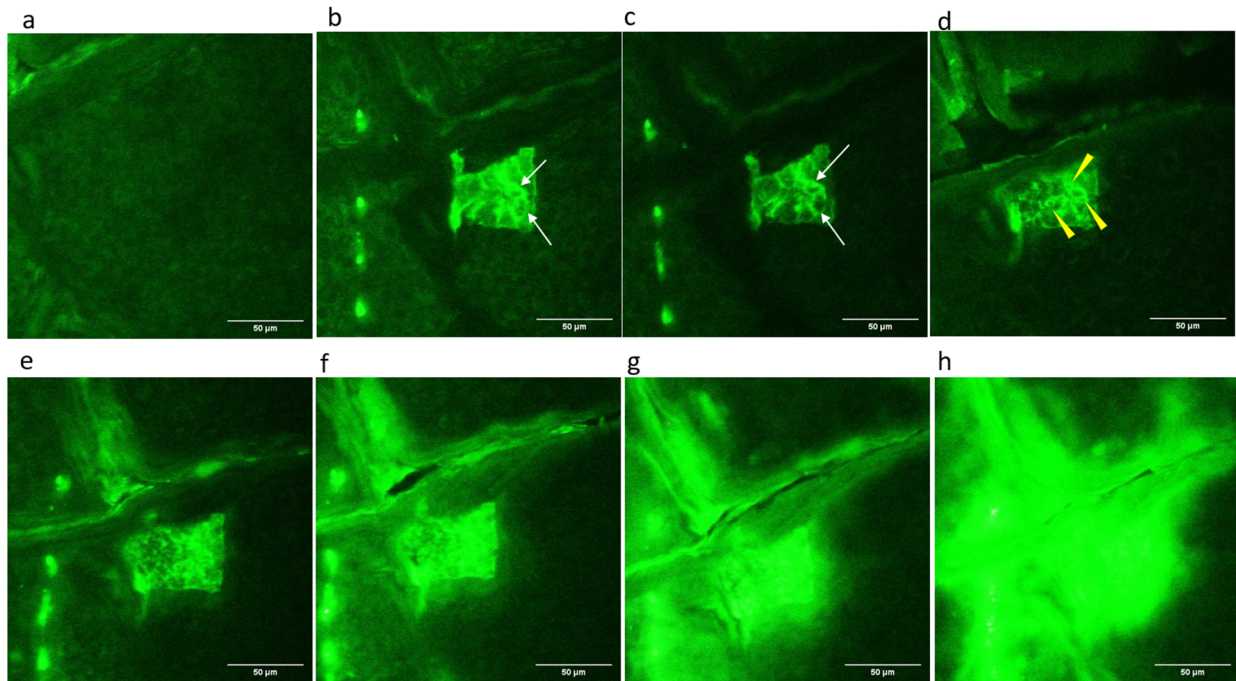


Figure 3. 1 In vivo En-face MPM images of epidermis (laser exposure generated in the Stratum Spinosum) at different time points at different layers. (a) before, (b) right after, (c) 3-hours, (d) day 1, (e) day 3, (f) week 1, (g) week 2, (h) week 4. These are pseudo-colored images. Green color represents the TPF signals. Scale bar represents 50 μm in all MPM images. Excitation wavelength: 750 nm. Image dimension: 200 μm \times 200 μm . White arrow (figure 3.1 b and c): individually injured keratinocytes, displayed enlarged cell size and cell nuclei. Yellow arrow head (figure 3.1 d): small membrane bound vesicles, presumably due to vacuolization or membrane blebbing.

The vertical section images of the targeted area were shown in Figure 3.2. The skin alteration (distinguished by enhanced TPF fluorescent) was captured immediately after the laser thermolysis. The targeted site was localized to the stratum spinosum layer, and the layers above and below the targeted depth were unaffected, confirming the precision of multiphoton-thermolysis (Figure 3.2 b). The blurring of the targeted site in Figure 3.2b at the immediately after exposure time point was due to volunteer movement during the imaging session. At day 1, the

targeted site seemed to be slightly disbursed, corresponding to the spilling of cellular contents observed in the en face images (Figure 3.1 d). Moreover, a clear upward migration of the exposed tissue can be identified, indicating cells in the basal layer were probably proliferating and pushing the targeted tissue toward the skin surface (Figure 3.2 d). This upward migration continued at later time points. At week 1, the altered tissue was located just underneath the superficial stratum corneum. At later time points (Figure 4.2 f, g, and h), the epidermis showed strong TPF fluorescence. This observation can be explained by the application of a bandage aimed to protect the skin surface marker from frictional damage generated by daily activities. Dead keratinocytes (mainly keratin) accumulate at the skin surface, resulting in a strong fluorescence signal.

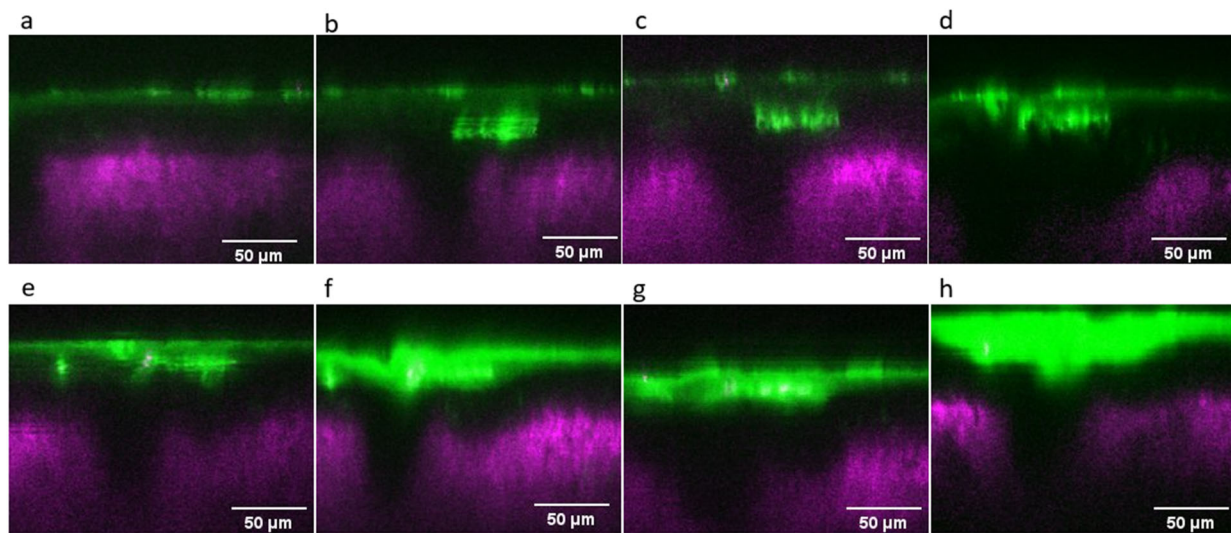


Figure 3. 2 Cross-sectional images of the laser exposed site at the stratum spinosum layer at different time points. (a) before, (b) immediately after, (c) 3 hours after, (d) day 1, (e) day 3, (f) week 1, (g) week 2, (h) week 4. These are pseudo-colored images. Green: TPF signal, Magenta: SHG signal. Scale bar represents 50 μm in all MPM images. Excitation wavelength: 810 nm. Image dimension: 200 μm \times 150 μm

Laser exposure in the basal layer

The laser targeted site was located in the stratum basale for two volunteers. The MPM epidermal response after multiphoton thermolysis is shown in Figure 3.3. Before the laser thermolysis, the keratinocytes at the basal layer showed normal distribution and morphology. As cells in the basal layer are more active and relatively undifferentiated, these keratinocytes are in general smaller in size compared to those in the spinosum layer. They appear as bright fluorescent cells (Figure 3.3 a). MPM images revealed that after laser thermolysis, the targeted area showed significant increased fluorescence intensity; individual injured cells can be distinguished by enlarged cell size and nuclei compared to neighboring untargeted cells (Figure 3.3 b and c, white arrow). By day 1, injured cells had lost their membrane integrity. At this time, no cellular structure can be identified in the laser exposed area (Figure 3.3 d). Intracellular content was spilled out and spread to surrounding tissue, and the targeted area increased in size and became round in shape, this observation could be possibly explained by the process termed “passive bystander effect” (see discussion section). At day 3, the targeted area showed a decrease in size with migration into the stratum granulosum (characterized by the larger surrounding healthy keratinocytes). At this time point, clusters of MEND were the major content of the targeted area. As the altered area migrated upward toward the skin surface, its shape and structure were maintained throughout the rest of the measurements time point. By week 2, the altered area had been localized in the stratum corneum layer, characterized by the surrounding hexagon shaped corneocytes (Figure 3.3 g). At week 4, the altered area has not yet been completely exfoliated from the skin surface; part of the MEND still remained in the stratum corneum.

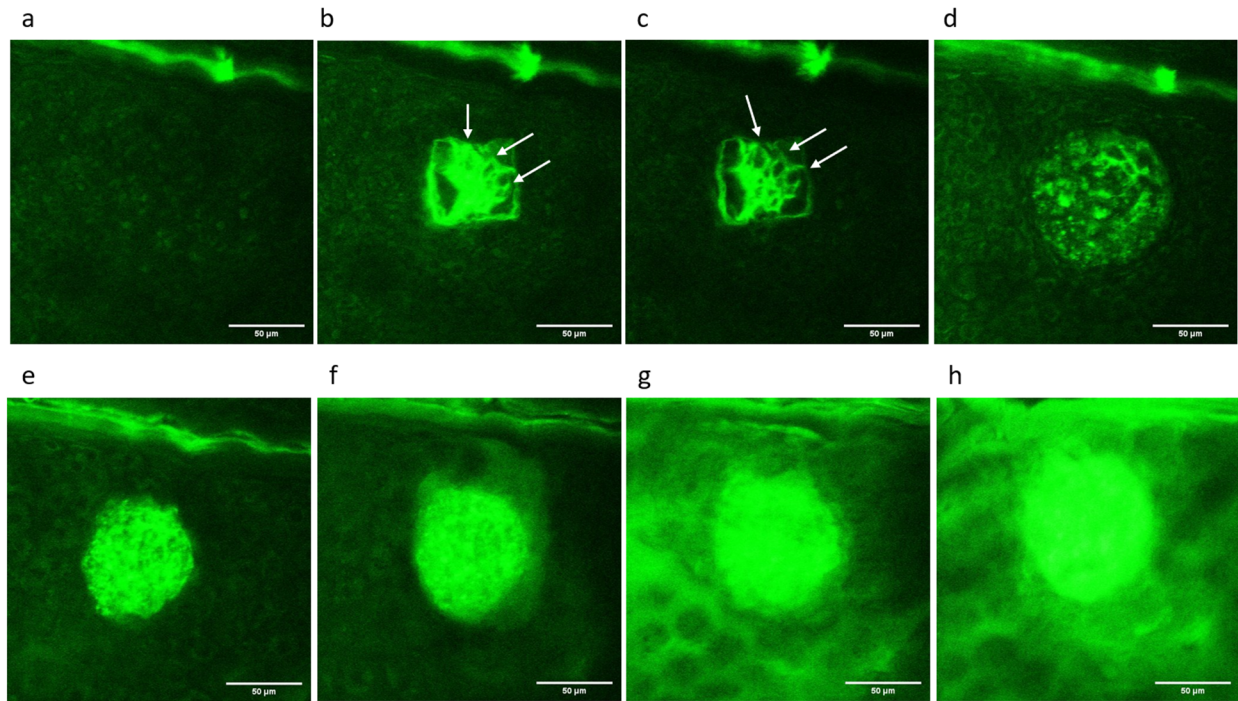


Figure 3.3 In vivo En-face MPM images of epidermis (laser exposure generated in the Stratum Basale) at different time points at different depths. (a) before, (b) after, (c) 3-hour, (d) day 1, (e) day 3, (f) week 1, (g) week 2, (h) week 4. These are pseudo-colored images. Green color represents the TPF signals. Scale bar represents 50 μm in all MPM images. Excitation wavelength: 750nm. Image dimension: 200 μm \times 200 μm White arrow: individual injured keratinocytes, with enlarged cell size and nuecli.

Vertical section images of the laser exposure site at the basal layer were shown in Figure 3.4. The alteration in the epidermis was also captured immediately after the thermolysis. MPM images revealed that the altered area showed a significant increase in the TPF fluorescence intensity. In contrast to the targeted site when the laser exposure was located in the spinosum layer, the affected area at the basal layer was thicker (Figure 3.4 b), indicating the energy absorbed by the targeted cells had diffused to tissue immediately above or below the targeted plane. This may be due to the presence of a strong chromophore, such as higher melanin content due to the presence

of melanocytes within the basal layer. The MPM image at day 1 after the laser thermolysis presented a clear upward migration of the targeted area. At this time point, clusters of small cells (Figure 3.4 d, red circle) were observed at close proximity of the lower boundary of the targeted area. These are probably inflammatory cells (small lymphocytes) infiltrated from the dermis. These inflammatory cells can be identified based on their morphological size and scattered distribution[65]. At day 3, the altered area showed a decrease in size and thickness, and the presumed inflammation was no longer apparent (Figure 3.4 e). MEND was the major content that occupied this region. At later measurement time points, the MEND continued to migrate upward. At week 2, the MEND had been partially exfoliated from the skin surface, the altered region was reduced in size and thickness (Figure 3.4 g). By week 4, the majority of the MEND was shed off with a small portion of it still remaining in the stratum corneum (Figure 3.4 h).

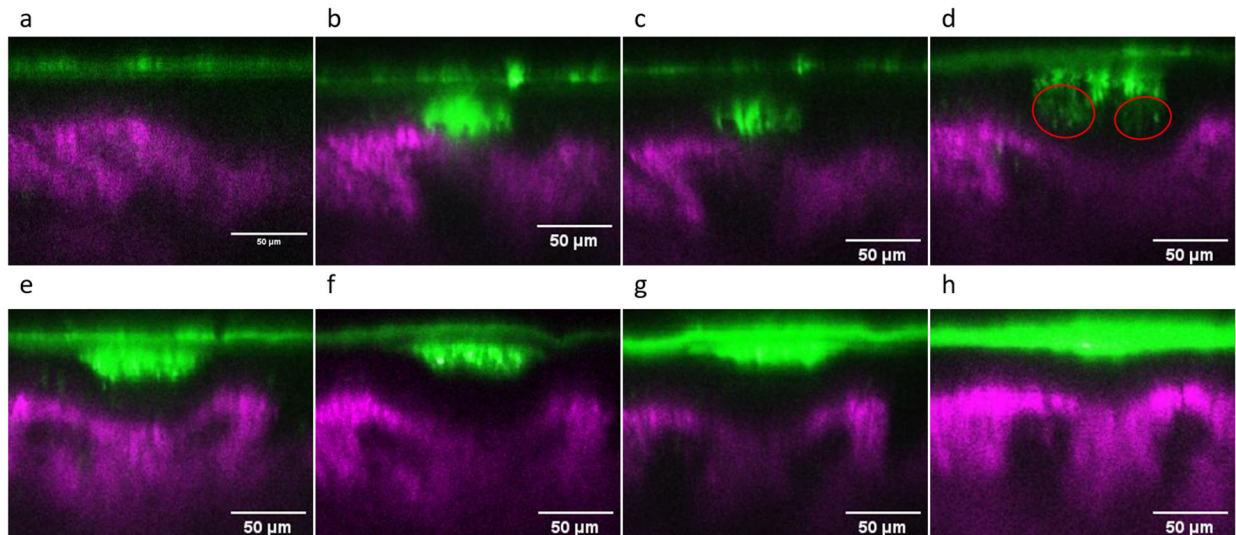


Figure 3. 4 Cross-sectional images of the laser exposed site at the stratum basale layer at different time points. (a) before, (b) immediately after, (c) 3 hours after, (d) day 1, (e) day 3, (f) week 1, (g) week 2, (h) week 4. These are pseudo-colored images. Green: TPF signal, Magenta: SHG signal. Scale bar

represents 50 μm in all MPM images. Excitation wavelength: 810 nm. Image dimension: 200 μm \times 150 μm . Red circle: likely inflammatory cells in close proximity to the targeted region.

Discussion

In this study, we evaluated the ability of multiphoton-thermolysis to generate precise skin alteration and the ability of MPM to capture *in vivo* skin dynamics after this laser exposure. With the current laser setting, epidermal alteration was successfully induced. In contrast to currently used clinical laser therapy, such as CO₂ ablative laser and fractional photothermolysis, this method does not evaporate the skin tissue. Instead, a photothermal effect was induced intraepidermally, and tissue surrounding the targeted area was left unaffected. This allowed us to monitor the detailed tissue alteration including necrosis, inflammation, and exfoliation of the debris using MPM at different time points over a 4-week period with potentially lower risks of open wounds and infections.

MPM imaging was able to identify tissue alteration immediately after the laser exposure, characterized by an enhanced TPF fluorescence in the targeted area. This enhancement of TPF after laser irradiation is consistent with earlier findings in various cell types[29, 65, 67-71], and can be used as an intrinsic indicator of photodamage of cells and tissues[72]. However, the source of the enhanced TPF signal is not yet fully understood or addressed. There are several possible explanations for this observed phenomenon. First, necrotic cells have been evidenced to exhibit increased autofluorescence, and studies have suggested that this is related to a decreased metabolic activity[73]. NADH is one of the major fluorophores for TPF signals in cells. As a cell undergoes mitochondrial respiration, NADH is oxidized to NAD. Any inhibition of the respiratory processes would lead to a build up of intracellular NADH concentration and hence increase the TPF

fluorescence intensity. Liang and colleagues demonstrated that when yeast cells were treated with H_2O_2 , necrosis or apoptosis was induced in those damaged cells, the intracellular NADH concentration and fluorescence intensity showed a significant increase[74]. This might have indicated that during the early phase of necrosis, the temporary inhibition of the cellular respiration processes resulted in a buildup of intracellular NADH which, at least partially, contributed to the enhancement of TPF signal intensity. Second, protein denaturation might also account for this TPF signal enhancement, as proteins may exhibit fluorescence on denaturation. There are several naturally fluorescent amino acids, such as tyrosine, tryptophan, and phenylalanine. Protein containing these amino acids might be expected to fluoresce when excited with UV light. However, such protein fluorescence was absent or significantly reduced due to fluorescence-self quenching of these amino acids by the nature of their immediate environment via various mechanisms[75]. Thus, the unfolding of the polypeptide chains during protein denaturation upon cell necrosis would be expected to change the micro-environment of these amino acids residues and reduce the self-quenching effect, resulting in an increase in fluorescence intensity[76]. Other studies showed that the MEND itself was fluorescent [65]. Balu and colleagues treated the forearm skin of a volunteer with a picosecond fractional laser. After 1 week following the laser treatment, they successfully imaged the MEND across the targeted epidermis. Histology graphs revealed that the MEND was mainly composed of keratinocyte cell fragments and a substantial amount of melanin[66], which displays strong fluorescent properties upon excitation. The MEND can be considered as a shuttle for cell fragments and melanin, which will be removed at the skin surface. Our observation was consistent with their finding. As the major mechanism of clearing of MEND in epidermis was by exfoliation, the debris we imaged with enhanced fluorescence intensity was apparent until being shed off at later observational time points.

Lasers have been widely used in various optical microscopes to achieve better visualization of cells and tissues *in vivo*. However, the excitation power has to be carefully monitored, as above a certain power threshold the laser exposure may influence cellular metabolism and lead to complete cell destruction including fragmentation[77]. In this work, the multiphoton-thermolysis utilized the same basic concept as multiphoton microscopy, namely that only at the focal point of a tightly focused laser beam would the photon density would be sufficient for multiphoton absorption to achieve precise microscopic tissue alteration. In order to generate sufficient tissue alteration by multiphoton-thermolysis, we used a 780 nm exposure wavelength with 200 mW laser power. The exposure time was 4 s, controlled by a programmable shutter. This resulted in a total of 800 mJ energy delivered into a $50\ \mu\text{m} \times 50\ \mu\text{m}$ area in the epidermis. With the concept of two-photon absorption, the 780 nm excitation wavelength was equivalent to a 390 nm single photon excitation, which lies within the UV-A range of the light spectrum. The laser energy was absorbed by strong chromophores such as melanin, NADH, and FAD in the epidermis. The temperature increased inside the targeted area and a photothermal effect was induced. In our results, the MPM images acquired immediately after the laser exposure revealed the enlargement of the cells and their nuclei in all the volunteers regardless of the depth of the laser exposure site (in the spinosum layer or in the basal layer) (Figure 3.1 b and Figure 3.3 b). The rupture of plasma membrane was observed at day 1. At this time point, no clear cellular structures can be identified in the targeted area. In addition, at day 1, presumed vacuolization or membrane blebbing processes was observed, as small membrane bound vesicles (Figure 3.1 d, yellow arrowhead) were captured under MPM. These observations were consistent with the typical characteristics of oncosis[78, 79], which is a form of cell death accompanied by cellular swelling, blebbing, increased membrane permeability, and simultaneous protein denaturation. It evolves to typical necrosis within 24 hours[80]. The

rapture of the cell membrane and the loss of cellular structure we imaged at day 1 indicated the complete cell death of those individually injured keratinocytes. Other than the photothermal effect, photochemical effect such as photooxidation may also play a role in generating cellular alterations. Unlike UVB and UVC, which can be directly absorbed by DNA and cause genotoxic damage to DNA, UVA induces DNA damage by exciting other endogenous chromophores which would generate reactive oxygen species (ROS) in cells[81]. For example, porphyrins, a endogenous photosensitizer, can generate singlet oxygen as a result of absorption of UVA radiation[82]. In addition, due to their abundance and carrying of photosensitizer groups, proteins are also major targets for photooxidation. Due to aromatic amino acids, most proteins can absorb radiation in the 250-320 nm region. Some proteins carrying prosthetic group, such as flavins and hemes, can absorb in the UVA range[83]. Photooxidation may occur from the absorption of the radiation by protein or their bounded groups, generating free radicals. These ROS can cause direct injury to proteins, lipids, and nucleic acids, leading to cell death. For example, protein oxidation will lead to the impairment of various enzymatic processes that can result in significant cellular dysfunction; Lipid oxidation will markedly affect the membrane integrity and linked with cell death; DNA strands break can be induced by oxidation, and leading to necrosis or maladaptive apoptosis[84]. These two possible mechanisms of generating tissue alteration are not mutually exclusive, however, which mechanism may be dominating in the generation of cellular alteration by multiphoton-thermolysis is yet to be studied. Since the production of ROS cannot be directly visualized in our MPM images, future experiments should be designed to validate the potential of photooxidation effect after the laser exposure.

When the laser thermolysis was located in the basal layer of epidermis, we observed more pronounced changes at day 1. At this time point, cells in the targeted area undergoes necrosis,

where they have lost their membrane integrity. The targeted area displayed an increase in size and became round in shape (Figure 3.3 d). This observation can be explained by a process termed “passive bystander effect”. The term bystander effect describes the ability of irradiated cells to send signals and to induce damage in surrounding unirradiated normal cells[85]. Due to membrane leakage, certain cellular debris, including lysosomes, are released in a disordered and unprocessed fashion, possibly damaging surrounding healthy keratinocytes and amplifying the tissue alteration in the targeted area[86]. As this effect was initiated from the center of targeted tissue and spread to the surrounding with a concentration gradient, the altered region displayed rounded shape after day 1. However, when the laser exposure was in the stratum spinosum, such enlargement and rounding of the targeted area was not observed (Figure 3.1 d). This can be partially explained by the fact that due to the presence of melanocytes in the basal layer of epidermis, laser energy was more efficiently absorbed by these strong absorbers. The photothermal effect diffused to tissue immediately above or below the targeted plane, leading to more severe tissue alterations and more extensive injury to the targeted cells. Future studies could aim to measure the temperature changes in the targeted area during and after the multiphoton-thermolysis to determine why there are differences in the skin dynamics after laser exposure at different depth.

3.1.2 Dermis

In this study, we also aimed to generate dermal alteration using multiphoton-thermolysis. The targeted area was reduced to $20\ \mu\text{m} \times 20\ \mu\text{m}$. Other exposure parameters were the same as epidermal exposure. The wavelength was set to 780 nm, laser power was 200 mW with 4 s exposure time. Despite we reduced the targeted area to increase the power density, only one of the five volunteers showed response to this multiphoton-thermolysis laser exposure, as visualized by

MPM images displayed in Figure 3.5. These images were acquired with excitation wavelength of 810 nm and were pseudo-colored such that the green represents the TPF signal, whereas the magenta represents the SHG signal from collagen. As figure 3.5a indicated, before the laser exposure, the major image signal generated in the dermis was from SHG signal, indicating that the dermis was mainly composed of collagen. Figure 3.5b presents the immediate dermal response after laser exposure. In the targeted region, the SHG signal demonstrated a clear decrease in the intensity, leaving a black space in the MPM images, and the TPF signal inside the targeted region was increased (white dashed line). The enhanced TPF signal was maintained with gradual decrease in intensity over the following measurements time points. No obvious dermal remodeling processes was imaged during the first 2-week measurement. At week four, the black space of the SHG signal became larger and more cellular structure with TPF fluorescence can be observed within the black space (Figure 3.5 h, red circle). This is probably due to fibroblasts' migration into the targeted region and the digestion of the altered collagen for future new collagen deposition.

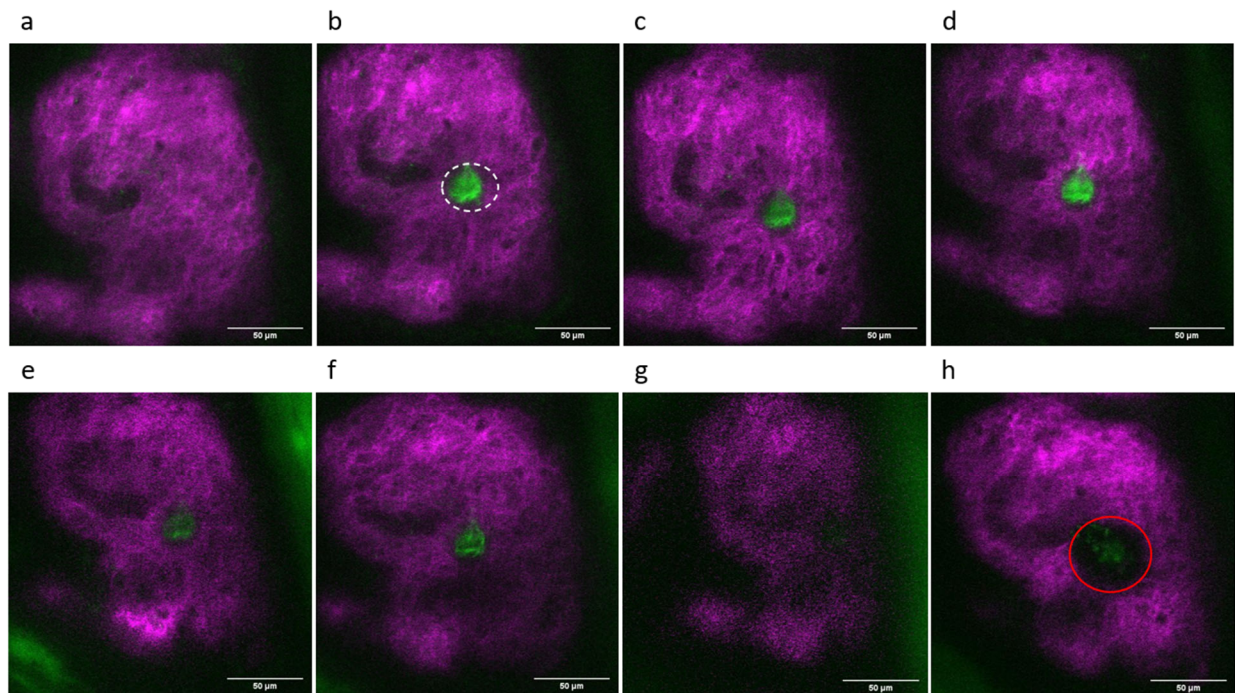


Figure 3. 5 En-face MPM images of the targeted site located in dermis. (a) before, (b) immediately after, (c) 3 hours after, (d) day 1, (e) day 3, (f) week 1, (g) week 2, (h) week 4. These are pseudo-colored images. Green: TPF signal, Magenta: SHG signal (collagen). Scale bar represents 50 μm in all MPM images. Excitation wavelength: 810nm. Image dimension: 200 μm \times 200 μm . White dashed line: targeted region, showed decrease in SHG signal and increase in TPF signal. Red circle: Cellular structure, fibroblasts migrated into the targeted region.

Figure 3.6 displays the cross-sectional MPM images acquired at the laser exposed site over time. Normal epidermis (green) and dermis (magenta) was shown in Figure 3.6a. Immediately after the laser exposure, denatured collagen is demonstrated in the targeted area, with decreased SHG signal and increased TPF signals (Figure 3.6b). These images also demonstrated the precision of multiphoton-thermolysis, as the epidermal and dermal tissue above or below the targeted site was left unaffected. Unlike the epidermis, the targeted region with the tissue debris did not migrate upward. Instead, it remained at the location where it was first generated (Figure 3.6 b-h). At week 4, the region with decreased SHG signal was expanded, and small cellular structure with green fluorescent was observed inside this area (Figure 3.6h, red circle), demonstrating the laser induced dermal remodeling processes. At the 2-week time point (Figure 3.6 g), the strong increase in TPF fluorescence intensity in the stratum corneum was also due to the application of the bandage to protect the skin surface marker, which may lead to the accumulation of dead keratinocytes. This increase in TPF was alleviated by cleaning the skin surface with alcohol wipes before measurement at week 4 (Figure 3.6 h).

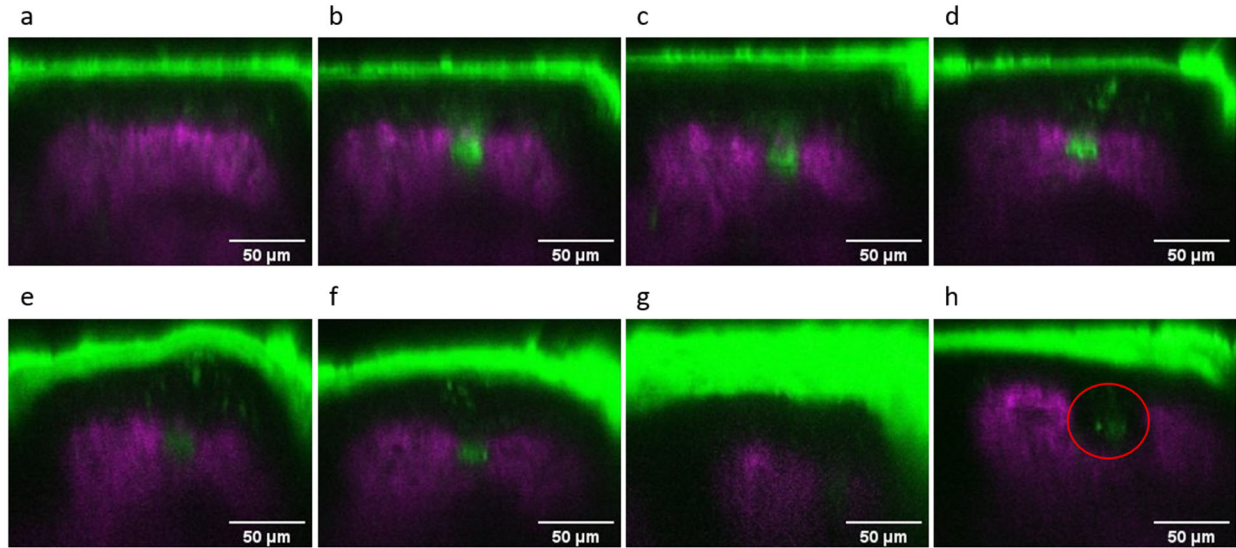


Figure 3. 6 Cross-sectional MPM images of the targeted site in dermis. (a) before, (b) immediately after, (c) 3 hours after, (d) day 1, (e) day 3, (f) week 1, (g) week 2, (h) week 4. These are pseudo-colored images. Green: TPF signal, Magenta: SHG signal. Scale bar represents 50 μm in all MPM images. Excitation wavelength: 810nm. Image dimension: 200 μm \times 150 μm . Red circle: Cellular structure, fibroblasts migrated into the targeted region.

Discussion

In this section, we used the multiphoton-thermolysis technique to generate tissue alteration in the dermis region. As Figure 3.5a and Figure 3.6a displayed, the targeted region was primarily composed of collagen. The increase in TPF and decrease in SHG within the targeted dermis region demonstrated immediate collagen denaturation after the laser exposure. It is well known that the SHG signal is generated from the triple helix molecular structure of collagen. This significant decrease in the SHG signal of the laser exposure site suggested a thermal alteration of the collagen conformation, from triple helices into random coils. [87]. One study suggested that the presence of a bityrosine structure after collagen thermal denaturation may contribute to the increase in TPF

signal[88]. However, in our previous experiments on murine skin, the emission spectra after laser exposure had a broad peak around 575 nm, which is very different from the sharp tyrosine fluorescence peak at 408 nm [29]. We previously proposed that this TPF could be attributed to carbonization of the targeted tissue, since large vacuoles were observed which indicated that temperature in the targeted area was over 100°C, and the emission spectra was similar to the carbon nanoparticles. In this work, the vacuoles were not observed in the targeted dermis region, and human epidermis is almost twice the thickness of mouse epidermis, which may result in more attenuation as the laser light passes through the epidermis[89]. As a result, the temperature in the targeted area of this region may not reach 100°C. Thus, the reason for the increase in TPF signal remains unclear. In the future, our system could be modified so that the temperature of the laser exposure site could be monitored simultaneously as we acquire the MPM images; this could help us confirm the identity of the source of the increased TPF signal after laser exposure.

For many currently used clinical skin resurfacing laser techniques, dermal remodeling is thought to be the primary contributor for rhytid reduction and skin texture improvement. This remodeling process includes the clearing of denatured old collagen and neosynthesis of collagen by fibroblasts. At week 4, infiltration of the altered dermis by fibroblasts were imaged as shown in Figure 3.5 h and Figure 3.6 h. At this time, the region with decrease SHG signal showed an outward expansion to the surrounding. This expansion can be attributed to the autolysis and removal of the altered collagen. It is necessary for this process to happen in order to initiate the deposition of new collagen in the dermis, as collagen fragments and partially degraded collagen inhibit their own biosynthesis [90, 91]. Metalloproteinases (MMPs) refer to a family of enzymes that can break down proteins, include collagen, that are usually found in extracellular spaces. They are often involved in processes such as wound healing and angiogenesis. Some genetic analyses

have revealed that following thermal denaturation or laser exposure, tissue remodeling is characterized by significantly elevated MMPs mRNA levels [92-95]. These increases in the MMPs levels in the altered region may contribute to the expansion of the targeted region without SHG signal in the dermis, prior to the collagen neogenesis. Following these increase in MMPs levels, mRNA of procollagen I and procollagen III was also documented, marking the deposition of new collagen which is a major process during the remodeling phase[96]. However, in our study, the duration of the experiment only last for 4 weeks. Although we did capture the presumed autolytic processing of the old, altered collagen, the complete recovery of the targeted region by new collagen deposition was not imaged. This process is expected to be imaged if we extend the observation period. In addition, when the collagen was denatured thermally by laser exposure, (Figure 3.5 a), it is associated with a significant increase in the TPF signal. However, such increase in the TPF signal was not observed at week 4, when more collagen was degraded enzymatically by fibroblast secretions (Figure 3.5 h). The reason(s) for this difference is not yet understood and requires further investigation.

In this study, five volunteers were recruited and all of them received both epidermal and dermal laser exposure. Although all the volunteers showed tissue alteration in the epidermis, only one volunteer showed tissue alteration in the dermis, despite reducing the targeted region's area to increase the local laser irradiance. As the laser pass through the epidermis, a portion of the laser energy was absorbed by the chromophores such as NADH, FAD, melanin, and proteins such as keratin. In addition, tissue scattering also accounted for the attenuation of light. The energy reached the dermis was significantly reduced due to these absorptions, making it more difficult to alter the dermal tissues. In order to generate sufficient tissue alteration to promote the remodeling

processes, it will likely be necessary to increase the laser power or extend the exposure time for future experiments.

3.2 Image-Guided Micro-Raman Spectroscopy

In addition to MPM images which can display cellular morphological changes and tissue architectural modifications, the IMRS was incorporated into the imaging system to measure the biochemical changes after laser thermolysis. To measure the Raman signals from the laser exposed area, the system was switched to a continuous wave (CW) laser source with excitation wavelength of 785 nm, and the laser power was controlled between 30-40 mW. The RCM *in vivo* imaging was utilized to localize to the exact same laser exposed site at each time point of measurement. Here, in this thesis, we only presented the Raman spectra before, after, and at day 1 (Figure 3.7-Figure 3.10) following the laser thermolysis, because after day 1, strong autofluorescence at the exposed site significantly interfered with the Raman signal, making the results less reliable.

3.2.1 Epidermis

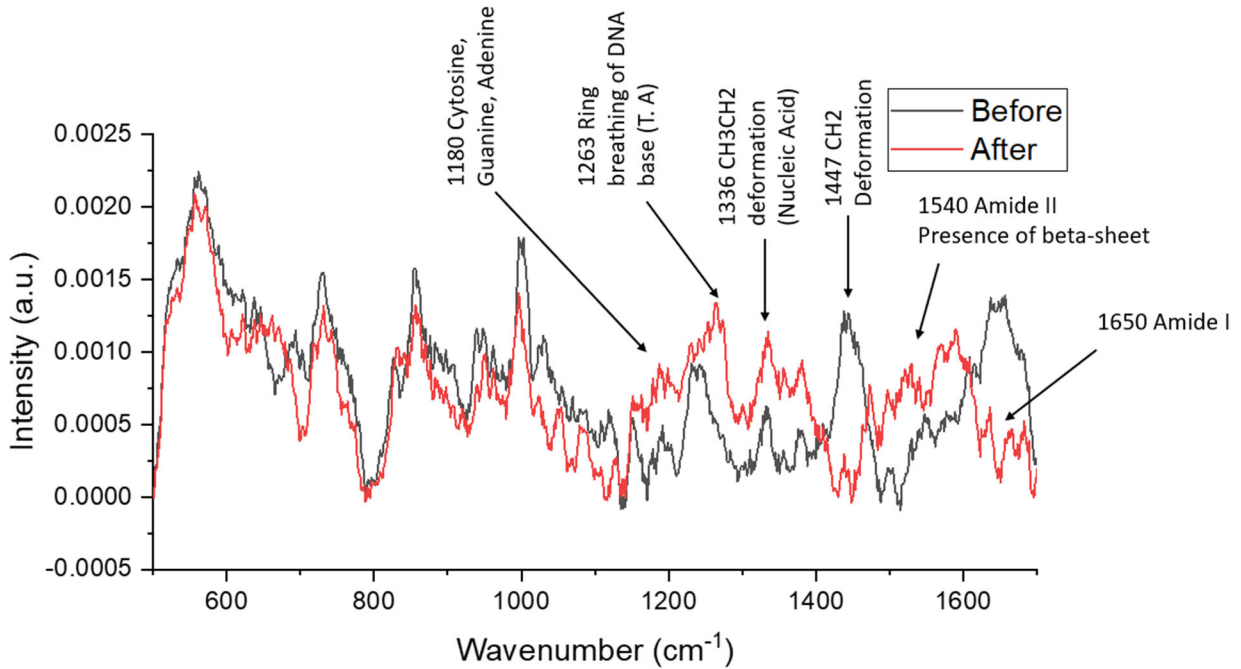


Figure 3. 7. Raman spectra at the laser exposed site in the epidermis before and after the laser exposure. Black line indicates the Raman signal before the laser exposure, and Red line indicates the Raman signal after the laser exposure. Raman measurements were excited with a Continuous wave laser at 785 nm. Laser power was controlled between 30-40 mW; the measurement dimension was 50 $\mu\text{m} \times 50 \mu\text{m}$. Spectrum was corrected to area under the curve.

Figure 3.7 presents the Raman spectra of the targeted site before and after the multiphoton-thermolysis. The Raman spectra of typical skin tissue is dominated by peaks related to proteins/amino acids, nucleic acids, and lipids/phospholipids [97]. The region of interest in this study showed normal skin Raman signal spectra before the laser thermolysis, with peaks related to the presence of proteins at 854, 941, 1002, 1269, 1450, and 1650 cm^{-1} , and peaks related to nucleic acids at 1180, 1263, and 1336 cm^{-1} (Figure 3.7, black line). Immediately after the laser thermolysis, significant changes in several of the major peaks were detected (Figure 3.7, red line).

The peak at 1450 cm^{-1} showed a major decrease in intensity. This peak is considered as a marker for protein concentration [98]. The observed decrease at this peak intensity indicated that a major decrease in the protein concentration was induced by the multiphoton-thermolysis. Moreover, the peak at 1650 cm^{-1} also decreased in intensity whereas the peak at 1540 cm^{-1} increased in intensity. The peak at 1650 cm^{-1} is assigned to $\nu\text{C=O}$ peptide bond in the amide I group of proteins, which indicates the presence of α -helix protein structure. And the peak at 1540 cm^{-1} is assigned to the $\nu\text{C-N}$ and $\delta\text{N-H}$ bond of amide II group, which indicates the presence of β -sheet confirmation of proteins [99]. Together, the changes in these peaks demonstrated that after the multiphoton-thermolysis, overall protein concentration within the targeted area was reduced, and the secondary structure of proteins was altered from α -helix to β -sheet. This observation provides support for our previous hypothesis, which proposed that the increased TPF intensity was partially due to the alteration or denaturation of protein structures.

In addition, peaks related to nucleic acid at 1180 , 1263 , and 1336 cm^{-1} showed marked increase, indicating an increase in cellular nuclear content. Under normal circumstances, cells have a relatively low level of transcription, and the chromatin is highly condensed and inactive, making it difficult to detect related Raman signals. DNA fragmentation may lead to a more open configuration of the chromatin, and the relative Raman intensity is expected to increase as a result [100]. Thus, this result suggested that after the laser thermolysis, an alteration of nucleic acid structure was also induced which will lead to necrosis or oncosis as previously described.

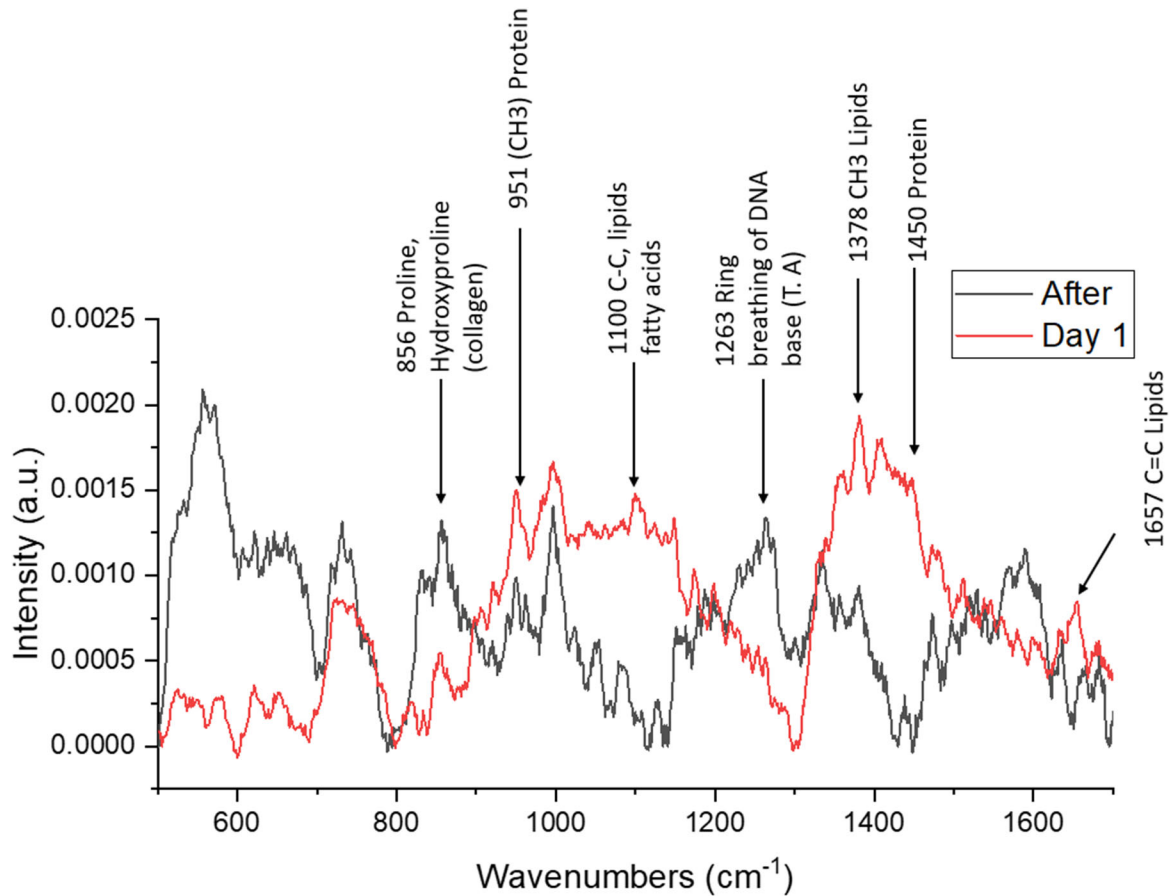


Figure 3. 8 Raman spectra at the laser exposed site in the epidermis immediately after and at day 1 following the laser exposure. Black line indicates the Raman signal immediately after the laser exposure, and red line indicates the Raman signal at day 1 following the laser exposure. Raman measurements were excited with a Continuous wave laser at 785 nm. Laser power was controlled between 30-40 mW, the measurement dimension was $50\ \mu\text{m} \times 50\ \mu\text{m}$. Spectrum were corrected to area under the curve.

The comparison of Raman signal immediately after and at day 1 after the laser exposure is presented in Figure 3.8. At day 1, peaks at $1100\ \text{cm}^{-1}$ ($\nu\text{C-C}$, lipids), $1378\ \text{cm}^{-1}$ (δCH_3 , lipid assignment), and $1657\ \text{cm}^{-1}$ (Fatty acid), all displayed an increase in their intensities. These increases in lipid content can be attributed to the increased production of lipid like

eicosanoids[101]. Eicosanoids are signaling molecules made from the oxidation of polyunsaturated fatty acids and are considered as major mediators of inflammation[102, 103]. Moreover, the release of fatty acid like arachidonic acids from cell membranes during inflammation may also contribute to these increases in lipid-related peaks. These findings suggested that at day 1 after laser exposure, the targeted region was involved in the inflammatory response which is consistent with our MPM images showing the infiltration of inflammatory cells (Figure 3.3 d and Figure 3.4 d). Other than these lipid like increase, peaks at 951 cm^{-1} and 1447 cm^{-1} that are related to protein concentrations also showed increased intensities. These changes suggested that at day 1, there seems to be rebound in the protein concentration. Previous study suggested that this increase in protein related Raman peaks is probably reflecting the production of proinflammatory proteinaceous molecules, TNF- α (tissue necrotic factor- α) and IL-1 β (interleukin-1 β), specifically[101]. In the study, when they used lipopolysaccharides, which are large molecules that promote the inflammatory response, to stimulate cultured monocytes, the Raman peak at 1447 cm^{-1} of stimulated monocytes was significantly higher than those inhibited cultures. Their suggestion was further confirmed with genetic analysis, which revealed that the mRNA levels of TNF- α and IL-1 β were both significantly higher in the stimulated monocytes cell culture. In addition, another study used human skin biopsy samples, acquired at different time points after laser treatment, also demonstrated statistically significant increase in the mRNA levels of both TNF- α and IL-1 β at first day posttreatment[96]. Together, these results revealed the induction of inflammatory responses at the targeted region after the multiphoton-thermolysis; and demonstrated the ability of our multimodality imaging system to detect biochemical changes at the microscopic level.

3.2.2 Dermis

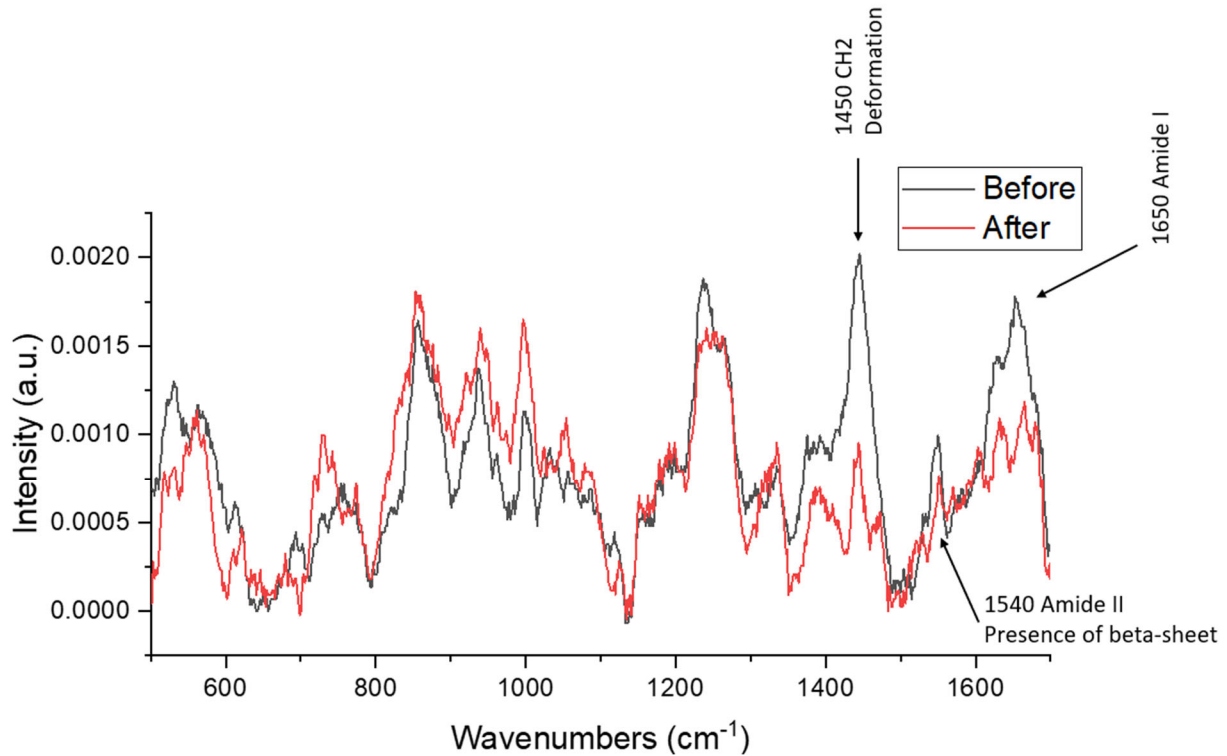


Figure 3. 9 Raman spectra at the laser exposed site in the dermis before and immediately after the laser exposure. Black line indicates the Raman signal before the laser exposure, and Red line indicates the Raman signal immediately after the laser exposure. Raman measurements were excited with a Continuous wave laser at 785 nm. Laser power was controlled between 30-40 mW; the measurement dimension was 50 $\mu\text{m} \times 50 \mu\text{m}$. Spectrum were corrected to area under the curve.

The Raman spectra of the targeted region in the dermis before and immediately after the laser exposure was presented in Figure 3.9. Similar to the epidermis, normal dermal Raman spectrum was detected before the laser exposure (Figure 3.9, black line), with peaks at 854, 941, 1002, 1269, 1450, and 1650 cm^{-1} related to the presence of proteins. And the decrease in overall protein concentration at 1450 cm^{-1} , and the change in protein secondary structure illustrated by the

decrease at 1650 cm^{-1} was also detected. However, the increase at 1540 cm^{-1} , which indicate the presence of β -sheet confirmation of protein, was not observed. This is probably due to the fact that collagen was the major protein present in the dermis, and as previously described, thermally altered collagen displays a conformation change from triple helices into random coil instead of β -sheet.

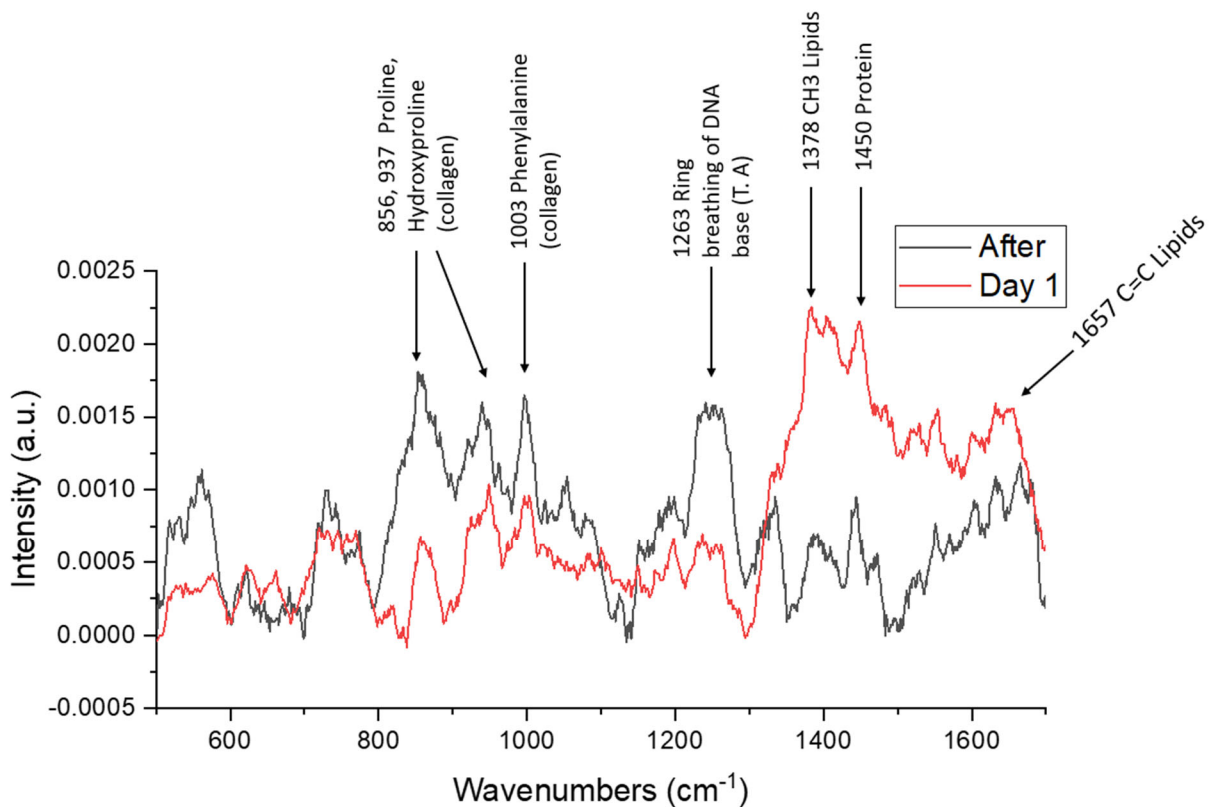


Figure 3. 10 Raman spectra at the laser exposed site in the dermis immediately after and at day 1 following the laser exposure. Black line indicates the Raman signal immediately after the laser exposure, and Red line indicates the Raman signal at day 1 following the laser exposure. Raman measurements were excited with a Continuous wave laser at 785 nm. Laser power was controlled between 30-40 mW; the measurement dimension was $50\ \mu\text{m} \times 50\ \mu\text{m}$. Spectrum were corrected to area under the curve.

The inflammatory response, including the increase in lipid-like content at 1100, 1378, and 1657 cm^{-1} ; and increase in protein-like content at 1147 cm^{-1} that were described in the epidermis section, was also observed in the dermis. However, three major decreases in peak intensities at 856, 937, and 1003 cm^{-1} were detected. The peak at 856 and 937 cm^{-1} can be assigned to proline and hydroxyproline of collagen origin. And the peak at 1003 cm^{-1} is also assigned to collagen. The decrease in these peak intensities demonstrated that the multiphoton-themrolysis successfully generated collagen denaturation and the inflammatory response was also initiated in the dermal targeted region.

3.3 Optical Redox Ratio

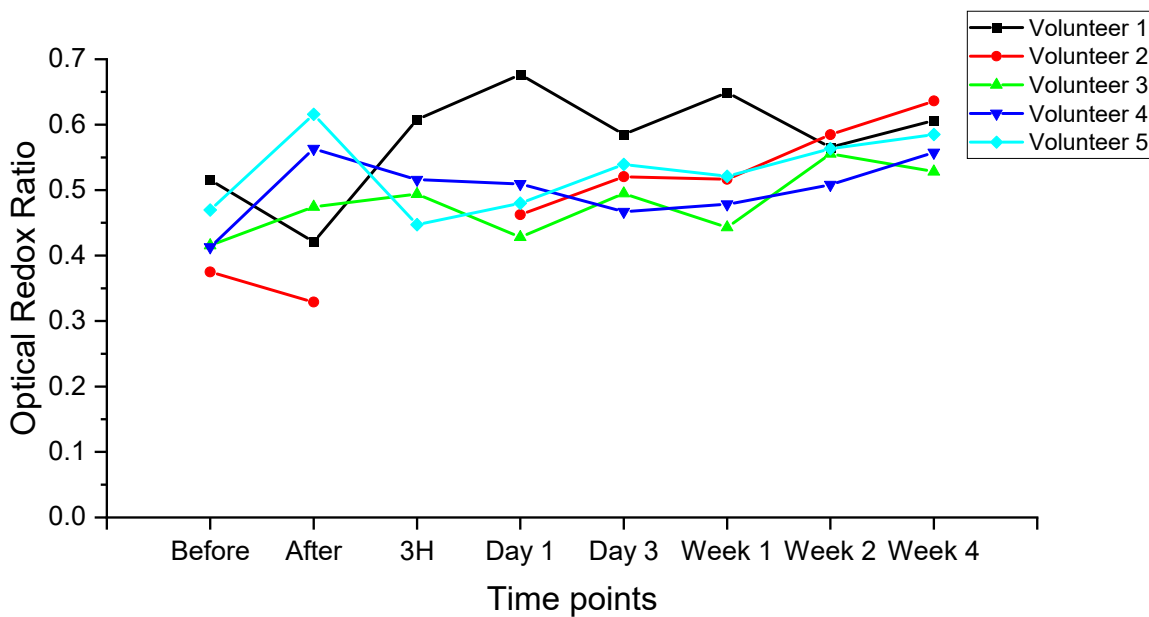


Figure 3. 11 Average redox ratio of the basal cell layer for each volunteer at different time points.

The Stratum Basale is the deepest cell layer of epidermis. It contains the melanocytes, Merkel cells, and the basal keratinocyte stem cells which have the ability to proliferate to provide new daughter cells to replace the old epidermis. Thus, it is expected that the cellular metabolism at the basal layer should be higher, especially after an injury to compensate for the loss of cells during the procedure. In this work, we aimed to compute the optical redox ration at the basal layer underneath the targeted region to quantify the skin dynamic response after laser thermolysis. Figure 3.12 shows the representative en-face images of the redox ratio at the basal layer of epidermis. The laser targeted region displayed a high redox ratio, indicates these cells are damaged and their metabolism is interrupted (Figure 3.12 a-d). At day 1, cells surrounding the targeted tissue showed more blue color which suggests that these neighboring cells had increased their metabolism to compensate for the alteration generated in the targeted region (Figure 3.12d). The average redox ratio was calculated based on the average of all the pixels in the image for each volunteer (Figure 3.11). It can be observed that there are large variations for each volunteer at the early timepoints. This is one limitation of this study. Since we only have five volunteers, the sample size is not big enough to generate statistically significant results. A future experiment with larger sample size might be necessary to get more accurate measure of the redox ratio, and to quantify the skin metabolic dynamics after the laser exposure. At later time points, there seems to be an increasing trend that is more consistent among different volunteers. During cellular metabolism, NAD^+ is reduced to NADH , and FAD is reduced to FADH_2 . So a higher redox ratio means lower cellular NADH and higher FAD content, which indicate a lower metabolic rate[58]. Thus, these increasing redox ratio reflected a decrease in the metabolism of the basal layer, probably indicating a decrease in the proliferation activity. These measurements of the redox ratio at later time points were consistent with our previous MPM images observation. During the early phase after laser

exposure (from immediately after to day 3), the upward migration of the targeted/altered tissue was clearly visible (Figure 3.2 and Figure 3.4), and the migration slowed down at later measurements time points.

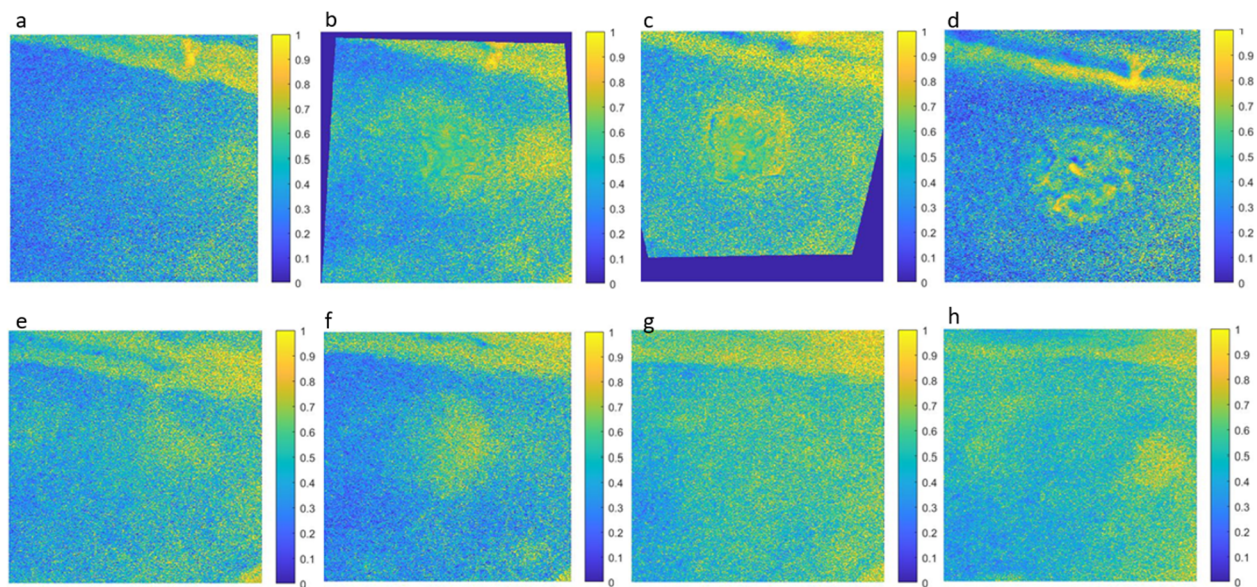


Figure 3. 12 Representative optical redox images of basal layer epidermis. (a) before, (b) immediately after, (c) 3 hours after, (d) day 1, (e) day 3, (f) week 1, (g) week 2, (h) week 4. These are pseudo-color images.

Yellow indicates high redox ratio which corresponds to low metabolic rate. Blue indicates low redox ratio, which represents high metabolic rate.

3.4 Conclusion

The first objective of this study is to test the ability of the multiphoton-thermolysis to generate tissue alteration in the epidermis and dermis of *in vivo* human skin. The MPM images we acquired right after the laser exposure, revealed that this technique successfully induced photothermal effects in the epidermis in all five volunteers, regardless of the depth of the targeted region. However, for the dermis experiment, with the current laser setting, the multiphoton-thermolysis only induced tissue alteration in one of the five volunteers. This could be a result of

light attenuation as it passes through the epidermal region. In future applications, in order to achieve more pronounced changes in the dermal region, we will have to increase the laser power or extend the exposure time. In addition, the MPM images acquired at different time points after the laser exposure revealed skin response that can be characterized in the inflammatory phase and remodeling phase of wound healing, suggesting that this multiphoton-thermolysis is able to generate tissue alteration and also to initiate a wound-healing like response in the skin. The second objective is to demonstrate the ability of our multimodality imaging system with image-guided micro-Raman spectroscopy (IMRS) to monitor the skin response dynamics after the laser exposure. From our results, the MPM images revealed 1) cellular morphological changes including oncosis, necrosis, and inflammatory infiltration; 2) tissue architectural modifications such as the dermal remodeling processes; and 3) the IMRS revealed biochemical. In addition, the optical redox was also measured to evaluate the cellular metabolic changes. The results revealed a general increase in metabolism during the early phase after the laser exposure, and a trend of decreased metabolism at later time points.

In terms of the potential application of these techniques in the future, the multiphoton-thermolysis may be applied to clinical treatment for conditions that require highly precise and non-invasive surgery. Since the tissue surrounding the targeted region was unaffected, specifically the epidermal region above the targeted plane, this method can relieve the patients from the risk of infection and social down time after receiving treatments. As for the MPM imaging system, it is widely accepted that sustained proliferative signaling is one of the major hallmarks of cancer. Normal cells are carefully managed in terms of cell number and cell growth. In contrast, tumor cells display deregulated signaling cascades that will lead to unlimited growth, which will result in abnormal cellular morphology, tissue structural alteration, and enhanced metabolism rate. In

contrast to conventional histology, which is the gold standard for current cancer diagnosis, the MPM imaging system can provide label free, real-time morphological information of the tissue at cellular level, without the need to process and biopsy the tissue. Cellular and tissue structural changes can be directly visualized *in vivo*. In addition, the incorporated micro-Raman system and the optical redox ratio measurement can provide biochemical information and metabolic information. Altogether, this imaging modality has a great potential in future application of real-time diagnosis and therapy of skin cancers and other cutaneous disorders where precise thermal alteration is desirable.

Bibliography

1. Mescher, A.L. and M. Access, *Junqueira's basic histology: text and atlas*. Fifteenth;15th; ed. 2018, New York: McGraw-Hill Education.
2. Sinno, H. and S. Prakash, *Complements and the wound healing cascade: an updated review*. *Plastic surgery international*, 2013. **2013**: p. 146764.
3. Miller, L.S., *Toll-like receptors in skin*. *Adv Dermatol*, 2008. **24**: p. 71-87.
4. Strbo, N., N. Yin, and O. Stojadinovic, *Innate and Adaptive Immune Responses in Wound Epithelialization*. *Advances in wound care*, 2014. **3(7)**: p. 492-501.
5. Brancato, S.K. and J.E. Albina, *Wound Macrophages as Key Regulators of Repair Origin, Phenotype, and Function*. *American Journal of Pathology*, 2011. **178(1)**: p. 19-25.
6. Sindrilaru, A. and K. Scharffetter-Kochanek, *Disclosure of the Culprits: Macrophages-Versatile Regulators of Wound Healing*. *Adv Wound Care (New Rochelle)*, 2013. **2(7)**: p. 357-368.
7. Rittie, L., *Cellular mechanisms of skin repair in humans and other mammals*. *Journal of Cell Communication and Signaling*, 2016. **10(2)**: p. 103-120.
8. Krawczyk, W.S., *A pattern of epidermal cell migration during wound healing*. *J Cell Biol*, 1971. **49(2)**: p. 247-63.
9. Pastar, I., et al., *Epithelialization in Wound Healing: A Comprehensive Review*. *Adv Wound Care (New Rochelle)*, 2014. **3(7)**: p. 445-464.
10. Reinke, J.M. and H. Sorg, *Wound repair and regeneration*. *Eur Surg Res*, 2012. **49(1)**: p. 35-43.

11. Ozgok Kangal, M.K. and J.P. Regan, *Wound Healing*, in *StatPearls*. 2020, StatPearls Publishing. Copyright © 2020, StatPearls Publishing LLC.: Treasure Island (FL).
12. Wietecha, M.S., W.L. Cerny, and L.A. DiPietro, *Mechanisms of vessel regression: toward an understanding of the resolution of angiogenesis*. *Curr Top Microbiol Immunol*, 2013. **367**: p. 3-32.
13. Bodnar, R.J., *Chemokine Regulation of Angiogenesis During Wound Healing*. *Adv Wound Care (New Rochelle)*, 2015. **4**(11): p. 641-650.
14. Gurtner, G.C., et al., *Wound repair and regeneration*. *Nature*, 2008. **453**(7193): p. 314-21.
15. Rohani, M.G. and W.C. Parks, *Matrix remodeling by MMPs during wound repair*. *Matrix Biol*, 2015. **44-46**: p. 113-21.
16. Altshuler, G.B., et al., *Extended theory of selective photothermolysis*. *Lasers Surg Med*, 2001. **29**(5): p. 416-32.
17. Bodendorf, M.O., et al., *Fractional laser skin therapy*. *J Dtsch Dermatol Ges*, 2009. **7**(4): p. 301-8.
18. Alexiades-Armenakas, M.R., J.S. Dover, and K.A. Arndt, *The spectrum of laser skin resurfacing: Nonablative, fractional, and ablative laser resurfacing*. *Journal of the American Academy of Dermatology*, 2008. **58**(5): p. 719-737.
19. Manstein, D., et al., *Fractional photothermolysis: a new concept for cutaneous remodeling using microscopic patterns of thermal injury*. *Lasers Surg Med*, 2004. **34**(5): p. 426-38.
20. Trivedi, M.K., F.C. Yang, and B.K. Cho, *A review of laser and light therapy in melasma*. *Int J Womens Dermatol*, 2017. **3**(1): p. 11-20.

21. Omi, T. and K. Numano, *The Role of the CO2 Laser and Fractional CO2 Laser in Dermatology*. Laser Ther, 2014. **23**(1): p. 49-60.
22. Anderson, R.R. and J.A. Parrish, *Selective photothermolysis: precise microsurgery by selective absorption of pulsed radiation*. Science, 1983. **220**(4596): p. 524-7.
23. Rinaldi, F., *Laser: a review*. Clin Dermatol, 2008. **26**(6): p. 590-601.
24. Heger, M., et al., *Towards optimization of selective photothermolysis: prothrombotic pharmaceutical agents as potential adjuvants in laser treatment of port wine stains. A theoretical study*. Thromb Haemost, 2005. **93**(2): p. 242-56.
25. Ibrahimi, O.A., et al., *Laser hair removal*. Dermatol Ther, 2011. **24**(1): p. 94-107.
26. Paithankar, D.Y., et al., *Acne Treatment Based on Selective Photothermolysis of Sebaceous Follicles with Topically Delivered Light-Absorbing Gold Microparticles*. J Invest Dermatol, 2015. **135**(7): p. 1727-1734.
27. Lanigan, S.W., *Incidence of side effects after laser hair removal*. J Am Acad Dermatol, 2003. **49**(5): p. 882-6.
28. Lim, S.P. and S.W. Lanigan, *A review of the adverse effects of laser hair removal*. Lasers Med Sci, 2006. **21**(3): p. 121-5.
29. Huang, Y., et al., *Precise Spatially Selective Photothermolysis Using Modulated Femtosecond Lasers and Real-time Multimodal Microscopy Monitoring*. Theranostics, 2017. **7**(3): p. 513-522.
30. Grajdeanu, I.A., et al., *Use of imaging techniques for melanocytic naevi and basal cell carcinoma in integrative analysis (Review)*. Exp Ther Med, 2020. **20**(1): p. 78-86.
31. Bhatta, A.K., U. Keyal, and Y. Liu, *Application of high frequency ultrasound in dermatology*. Discov Med, 2018. **26**(145): p. 237-242.

32. Crisan, M., et al., *Ultrasonographic staging of cutaneous malignant tumors: an ultrasonographic depth index*. Arch Dermatol Res, 2013. **305**(4): p. 305-13.
33. Podoleanu, A.G., *Optical coherence tomography*. J Microsc, 2012. **247**(3): p. 209-19.
34. Aumann, S., et al., *Optical Coherence Tomography (OCT): Principle and Technical Realization*, in *High Resolution Imaging in Microscopy and Ophthalmology: New Frontiers in Biomedical Optics*, J.F. Bille, Editor. 2019, Springer
Copyright 2019, The Author(s). Cham (CH). p. 59-85.
35. Calzavara-Pinton, P., et al., *Reflectance confocal microscopy for in vivo skin imaging*. Photochem Photobiol, 2008. **84**(6): p. 1421-30.
36. Shahriari, N., et al., *Reflectance confocal microscopy: Principles, basic terminology, clinical indications, limitations, and practical considerations*. J Am Acad Dermatol, 2021. **84**(1): p. 1-14.
37. Rajadhyaksha, M., et al., *In vivo confocal scanning laser microscopy of human skin: melanin provides strong contrast*. J Invest Dermatol, 1995. **104**(6): p. 946-52.
38. Busam, K.J., et al., *Detection of intraepidermal malignant melanoma in vivo by confocal scanning laser microscopy*. Melanoma Res, 2002. **12**(4): p. 349-55.
39. Langley, R.G., et al., *Confocal scanning laser microscopy of benign and malignant melanocytic skin lesions in vivo*. J Am Acad Dermatol, 2001. **45**(3): p. 365-76.
40. Gerger, A., et al., *In vivo confocal laser scanning microscopy in the diagnosis of melanocytic skin tumours*. Br J Dermatol, 2009. **160**(3): p. 475-81.
41. Li, X., et al., *Spectrum- and time-resolved endogenous multiphoton signals reveal quantitative differentiation of premalignant and malignant gastric mucosa*. Biomed Opt Express, 2018. **9**(2): p. 453-471.

42. Svoboda, K. and R. Yasuda, *Principles of two-photon excitation microscopy and its applications to neuroscience*. Neuron, 2006. **50**(6): p. 823-39.
43. König, T.T., J. Goedeke, and O.J. Muensterer, *Multiphoton microscopy in surgical oncology- a systematic review and guide for clinical translatability*. Surg Oncol, 2019. **31**: p. 119-131.
44. Jain, M., et al., *Exploring Multiphoton Microscopy as a Novel Tool to Differentiate Chromophobe Renal Cell Carcinoma From Oncocytoma in Fixed Tissue Sections*. Arch Pathol Lab Med, 2018. **142**(3): p. 383-390.
45. Rogart, J.N., et al., *Multiphoton imaging can be used for microscopic examination of intact human gastrointestinal mucosa ex vivo*. Clin Gastroenterol Hepatol, 2008. **6**(1): p. 95-101.
46. Jain, M., et al., *Multiphoton microscopy: a potential intraoperative tool for the detection of carcinoma in situ in human bladder*. Arch Pathol Lab Med, 2015. **139**(6): p. 796-804.
47. Li, L., et al., *Multimodal multiphoton imaging for label-free monitoring of early gastric cancer*. BMC Cancer, 2019. **19**(1): p. 295.
48. Poulon, F., et al., *Real-time Brain Tumor imaging with endogenous fluorophores: a diagnosis proof-of-concept study on fresh human samples*. Sci Rep, 2018. **8**(1): p. 14888.
49. Williams, R.M., et al., *Strategies for high-resolution imaging of epithelial ovarian cancer by laparoscopic nonlinear microscopy*. Transl Oncol, 2010. **3**(3): p. 181-94.
50. Goedeke, J., et al., *Multiphoton microscopy in the diagnostic assessment of pediatric solid tissue in comparison to conventional histopathology: results of the first international online interobserver trial*. Cancer Manag Res, 2019. **11**: p. 3655-3667.

51. Perry, S.W., R.M. Burke, and E.B. Brown, *Two-photon and second harmonic microscopy in clinical and translational cancer research*. *Ann Biomed Eng*, 2012. **40**(2): p. 277-91.
52. Keikhosravi, A., et al., *Second-harmonic generation imaging of cancer*. *Methods Cell Biol*, 2014. **123**: p. 531-46.
53. Burke, K., P. Tang, and E. Brown, *Second harmonic generation reveals matrix alterations during breast tumor progression*. *J Biomed Opt*, 2013. **18**(3): p. 31106.
54. Devitt, G., et al., *Raman Spectroscopy: An Emerging Tool in Neurodegenerative Disease Research and Diagnosis*. *ACS Chem Neurosci*, 2018. **9**(3): p. 404-420.
55. Butler, H.J., et al., *Using Raman spectroscopy to characterize biological materials*. *Nat Protoc*, 2016. **11**(4): p. 664-87.
56. Eberhardt, K., et al., *Advantages and limitations of Raman spectroscopy for molecular diagnostics: an update*. *Expert Rev Mol Diagn*, 2015. **15**(6): p. 773-87.
57. Ralbovsky, N.M. and I.K. Lednev, *Raman spectroscopy and chemometrics: A potential universal method for diagnosing cancer*. *Spectrochim Acta A Mol Biomol Spectrosc*, 2019. **219**: p. 463-487.
58. Jones, J.D., et al., *Quantifying Age-Related Changes in Skin Wound Metabolism Using In Vivo Multiphoton Microscopy*. *Adv Wound Care (New Rochelle)*, 2020. **9**(3): p. 90-102.
59. Jones, J.D., et al., *In vivo multiphoton microscopy detects longitudinal metabolic changes associated with delayed skin wound healing*. *Commun Biol*, 2018. **1**: p. 198.
60. Xu, H.N., et al., *Optical Redox Imaging of Lonidamine Treatment Response of Melanoma Cells and Xenografts*. *Mol Imaging Biol*, 2019. **21**(3): p. 426-435.
61. Ostrander, J.H., et al., *Optical redox ratio differentiates breast cancer cell lines based on estrogen receptor status*. *Cancer Res*, 2010. **70**(11): p. 4759-66.

62. Alhallak, K., et al., *Optical redox ratio identifies metastatic potential-dependent changes in breast cancer cell metabolism*. Biomed Opt Express, 2016. **7**(11): p. 4364-4374.
63. Zhao, J., et al., *Automated autofluorescence background subtraction algorithm for biomedical Raman spectroscopy*. Appl Spectrosc, 2007. **61**(11): p. 1225-32.
64. Tian, Y., *Imaging the dynamics of skin responses to UV challenges using non-invasive in vivo microscopy*. 2020.
65. Balu, M., et al., *In vivo multiphoton-microscopy of picosecond-laser-induced optical breakdown in human skin*. Lasers Surg Med, 2017. **49**(6): p. 555-562.
66. Laubach, H.J., et al., *Skin responses to fractional photothermolysis*. Lasers Surg Med, 2006. **38**(2): p. 142-9.
67. Koester, H.J., et al., *Ca²⁺ fluorescence imaging with pico- and femtosecond two-photon excitation: signal and photodamage*. Biophys J, 1999. **77**(4): p. 2226-36.
68. Galbraith, J.A. and M. Terasaki, *Controlled damage in thick specimens by multiphoton excitation*. Mol Biol Cell, 2003. **14**(5): p. 1808-17.
69. Wang, H., et al., *Imaging directed photothermolysis through two-photon absorption demonstrated on mouse skin - a potential novel tool for highly targeted skin treatment*. J Biophotonics, 2014. **7**(7): p. 534-41.
70. Straub, M., *Multifocal multiphoton microscopy: A fast and efficient tool for 3-D fluorescence imaging*. Bioimaging. **6**(4): p. 177-185.
71. Pestov, D., et al., *Photobleaching and photoenhancement of endogenous fluorescence observed in two-photon microscopy with broadband laser sources*. Journal of Optics, 2010. **12**(8): p. 084006.

72. Galli, R., et al., *Intrinsic indicator of photodamage during label-free multiphoton microscopy of cells and tissues*. PLoS One, 2014. **9**(10): p. e110295.
73. Hennings, L., et al., *Dead or alive? Autofluorescence distinguishes heat-fixed from viable cells*. Int J Hyperthermia, 2009. **25**(5): p. 355-63.
74. Liang, J., et al., *Study the oxidative injury of yeast cells by NADH autofluorescence*. Spectrochim Acta A Mol Biomol Spectrosc, 2007. **67**(2): p. 355-9.
75. Majno, G., M. La Gattuta, and T.E. Thompson, *Cellular death and necrosis: chemical, physical and morphologic changes in rat liver*. Virchows Arch Pathol Anat Physiol Klin Med, 1960. **333**: p. 421-65.
76. Basak, S. and K. Chattopadhyay, *Studies of protein folding and dynamics using single molecule fluorescence spectroscopy*. Phys Chem Chem Phys, 2014. **16**(23): p. 11139-49.
77. König, K., et al., *Cellular response to near-infrared femtosecond laser pulses in two-photon microscopes*. Opt Lett, 1997. **22**(2): p. 135-6.
78. Majno, G. and I. Joris, *Apoptosis, oncosis, and necrosis. An overview of cell death*. Am J Pathol, 1995. **146**(1): p. 3-15.
79. Westman, J., S. Grinstein, and P.E. Marques, *Phagocytosis of Necrotic Debris at Sites of Injury and Inflammation*. Front Immunol, 2019. **10**: p. 3030.
80. Weerasinghe, P. and L.M. Buja, *Oncosis: an important non-apoptotic mode of cell death*. Exp Mol Pathol, 2012. **93**(3): p. 302-8.
81. D'Orazio, J., et al., *UV radiation and the skin*. Int J Mol Sci, 2013. **14**(6): p. 12222-48.
82. Vile, G.F. and R.M. Tyrrell, *UVA radiation-induced oxidative damage to lipids and proteins in vitro and in human skin fibroblasts is dependent on iron and singlet oxygen*. Free Radic Biol Med, 1995. **18**(4): p. 721-30.

83. Girard, P.M., et al., *UVA-induced damage to DNA and proteins: direct versus indirect photochemical processes*. Journal of Physics: Conference Series, 2011. **261**: p. 012002.
84. Auten, R.L. and J.M. Davis, *Oxygen toxicity and reactive oxygen species: the devil is in the details*. Pediatr Res, 2009. **66**(2): p. 121-7.
85. Purschke, M., et al., *Thermal injury causes DNA damage and lethality in unheated surrounding cells: active thermal bystander effect*. J Invest Dermatol, 2010. **130**(1): p. 86-92.
86. Dabrowska, A., M. Goś, and P. Janik, *"Bystander effect" induced by photodynamically or heat-injured ovarian carcinoma cells (OVPI0) in vitro*. Med Sci Monit, 2005. **11**(9): p. Br316-24.
87. Yeh, A.T., et al., *Imaging wound healing using optical coherence tomography and multiphoton microscopy in an in vitro skin-equivalent tissue model*. J Biomed Opt, 2004. **9**(2): p. 248-53.
88. Hovhannisyan, V., et al., *Dynamics of femtosecond laser photo-modification of collagen fibers*. Opt Express, 2008. **16**(11): p. 7958-68.
89. Gudjonsson, J.E., et al., *Mouse models of psoriasis*. J Invest Dermatol, 2007. **127**(6): p. 1292-308.
90. Fisher, G.J. and J.J. Voorhees, *Molecular mechanisms of photoaging and its prevention by retinoic acid: ultraviolet irradiation induces MAP kinase signal transduction cascades that induce Ap-1-regulated matrix metalloproteinases that degrade human skin in vivo*. J Invest Dermatol Symp Proc, 1998. **3**(1): p. 61-8.

91. Fisher, G.J., et al., *c-Jun-dependent inhibition of cutaneous procollagen transcription following ultraviolet irradiation is reversed by all-trans retinoic acid*. J Clin Invest, 2000. **106**(5): p. 663-70.
92. Orringer, J.S., et al., *Direct quantitative comparison of molecular responses in photodamaged human skin to fractionated and fully ablative carbon dioxide laser resurfacing*. Dermatol Surg, 2012. **38**(10): p. 1668-77.
93. Kim, J.E., et al., *Gene profiling analysis of the early effects of ablative fractional carbon dioxide laser treatment on human skin*. Dermatol Surg, 2013. **39**(7): p. 1033-43.
94. Tretti Clementoni, M., et al., *Random fractional ultrapulsed CO2 resurfacing of photodamaged facial skin: long-term evaluation*. Lasers Med Sci, 2013. **28**(2): p. 643-50.
95. Schmitt, L., et al., *Direct biological effects of fractional ultrapulsed CO2 laser irradiation on keratinocytes and fibroblasts in human organotypic full-thickness 3D skin models*. Lasers in Medical Science, 2018. **33**(4): p. 765-772.
96. Orringer, J.S., et al., *Dermal matrix remodeling after nonablative laser therapy*. J Am Acad Dermatol, 2005. **53**(5): p. 775-82.
97. Silveira, L., Jr., et al., *Normal-subtracted preprocessing of Raman spectra aiming to discriminate skin actinic keratosis and neoplasias from benign lesions and normal skin tissues*. Lasers Med Sci, 2020. **35**(5): p. 1141-1151.
98. Chan, J.W., et al., *Micro-Raman spectroscopy detects individual neoplastic and normal hematopoietic cells*. Biophys J, 2006. **90**(2): p. 648-56.
99. Anastassopoulou, J., et al., *Infrared and Raman Spectroscopic Studies of Molecular Disorders in Skin Cancer*. In Vivo, 2019. **33**(2): p. 567-572.

100. Stone, N., et al., *Raman spectroscopy for early detection of laryngeal malignancy: preliminary results*. Laryngoscope, 2000. **110**(10 Pt 1): p. 1756-63.
101. Mohan, M.C., A.P. Abhimannue, and B.P. Kumar, *Modulation of proinflammatory cytokines and enzymes by polyherbal formulation Guggulutiktaka ghritam*. J Ayurveda Integr Med, 2021. **12**(1): p. 13-19.
102. Jacob, J., et al., *Inhibition of proinflammatory pathways by bioactive fraction of *Tinospora cordifolia**. Inflammopharmacology, 2018. **26**(2): p. 531-538.
103. Garrelds, I.M., et al., *Time dependent production of cytokines and eicosanoids by human monocytic leukaemia U937 cells; effects of glucocorticosteroids*. Mediators Inflamm, 1999. **8**(4-5): p. 229-35.